



Interfacial electron interactions governed photoactivity and selectivity evolution of carbon dioxide photoreduction with spinel cobalt oxide based hollow hetero-nanocubes

Chao Cheng^{a,1}, Hengyue Xu^{b,1}, Maomao Ni^a, Changfa Guo^{a,*}, Yuanyuan Zhao^a, Yong Hu^{a,c,**}

^a Key Laboratory of the Ministry of Education for Advanced Catalysis Materials, Department of Chemistry, Zhejiang Normal University, Jinhua 321004, China

^b Tsinghua Shenzhen International Graduate School, Tsinghua University, Shenzhen 518055, China

^c College of Chemistry and Materials Engineering, Zhejiang A&F University, Hangzhou 311300, China

ARTICLE INFO

Keywords:

Co₃O₄
ZnIn₂S₄
Hollow hetero-nanocubes
Interfacial electron interactions
CO₂ photoreduction

ABSTRACT

In this work, an efficient CO₂ photoreduction catalyst based on Co₃O₄/ZnIn₂S₄ hollow hetero-nanocubes is precisely constructed via an in-situ transformation of cobalt-organic framework followed by a solvothermal reaction. Comprehensive in-situ spectroscopic analyses and theoretical calculations have revealed that the critical interfacial electron interactions (IEIs) effects on both photoactivity evolution and selectivity modulation in the Co₃O₄/ZnIn₂S₄ hetero-structure. As the content of ZnIn₂S₄ increases in the hetero-structure, the photoactivity exhibits a volcano-like evolution profile but the CH₄ selectivity reduces monotonously. The improved photoactivity is attributed to the IEIs-promoted charge separation as well as the specific-surface-area effect in terms of electron unitization rate, and the electronic structure of Co₃O₄ is tuned and the energy barrier for the key reaction intermediate *CHO is reduced, leading to improved CH₄ selection in comparison with bare Co₃O₄. The IEIs-mediated production selectivity is further verified by a Co₃O₄/CeO₂ heterojunction, indicating a certain universality of the IEI effect.

1. Introduction

Since the pioneering report in 1979 [1], photochemical conversion of CO₂ to valuable chemicals has been regarded as a promising solution to address the growing greenhouse effects and climate issues. Different with the case of polar H₂O molecules, the adsorption and activation of CO₂ molecules on semiconducting materials is relatively difficult, due to symmetry C=O bonds with a high dissolution energy of ~750 kJ mol⁻¹ [2]. Moreover, the reduction process of CO₂ involves multielectron-coupled proton transfer, variable reaction routes, and low product selectivity [3,4]. Till now, many inorganic and organic semiconducting materials have been proposed for CO₂ reduction, the photocatalysis efficiency and product selectivity are, however, insufficiently high, and far away from the practical level [5,6].

Many strategies have been put forward to improve CO₂ photoreduction activity of single semiconductors, such as size reduction, defect/strain engineering, built-in electric field modulation, heteroatom

doping, surface modification, construction of heterojunction (containing cocatalyst loading), use of hole scavengers [7–11]. Among which, heterojunctions made of two or more semiconductors with direct contact have been proven as one of the most effective approaches to promote photocatalysis efficiency, by virtue of charge transfer across interfaces and spatially separation of redox sites, which facilitates the separation of photogenerated carriers and suppresses backwards reactions [11]. The advantages of heterojunctions for photocatalysis are sufficiently exerted by direct Z-scheme systems, also called as S-scheme junctions, which has been paid considerable efforts to in the past decades [12,13]. For example, various S-scheme systems, such as TiO₂-, CdS-, and C₃N₄-based heterojunctions [14–16], have been successfully constructed, which exhibits significantly enhanced photoactivity towards CO₂ reduction in comparison with single-phase counterparts.

As two typical visible-light-response semiconductors, both Co₃O₄ and ZnIn₂S₄ have enough negative potentials for CO₂ reduction and thus were often employed to construct heterojunction photocatalysts, such as

* Corresponding author.

** Corresponding author at: College of Chemistry and Materials Engineering, Zhejiang A&F University, Hangzhou 311300, China.

E-mail addresses: changfa.guo@zjnu.edu.cn (C. Guo), yonghu@zjnu.edu.cn, yonghu@zafu.edu.cn (Y. Hu).

¹ These authors contributed equally to this work.

hollow $\text{Co}_3\text{O}_4/\text{NiCo}_2\text{O}_4$ hetero-nanocages [17], defective $\text{Co}_3\text{O}_4/\text{g-C}_3\text{N}_4$ hetero-nanosheets [18], $\text{Ag}/\text{CuO}/\text{ZnIn}_2\text{S}_4$ [19], and hollow core-shell $\text{Co}_3\text{S}_8 @ \text{ZnIn}_2\text{S}_4/\text{CdS}$ [20]. Compared to single semiconductors, heterojunctions significantly enhance photocatalytic CO_2 reduction activity. Moreover, their photocatalytic activity of heterojunctions takes a volcano-like evolution profile with monotonous change of component ratio, which is rationalized in terms of a compromise of enhanced carrier separation efficiency and light absorption capacity [17–24]. The enhanced carrier separation is associated with the interfacial electron interactions (IEIs) which creates interfacial built-in electric field driving carrier transfer in opposite directions. The role of IEIs is applied uniformly to all semiconductor heterojunction photocatalysts. However, the effects of IEIs on surface redox reactions have rarely been investigated. Additionally, theoretical calculations are usually employed to explain kinetic and thermodynamic properties of surface redox reactions for heterojunction photocatalysts. Furthermore, the structure model for theoretical calculations is generally constructed based on one component of heterojunctions [20,25]. Such simplification treatment might ignore the effects of IEIs how to influence on electronic structure of active sites and photoactivity.

Another interesting but often ignored phenomenon for heterogeneous photocatalysts is that product selectivity also functions as the components' ratio. For instance, Liu et al. found that the CO selectivity remarkably varies with the loading amount of sulfur vacancy-rich CuIn_5S_8 on $\text{g-C}_3\text{N}_4$ [26]. Similarly, O'Shea et al. reported the dependence of product selectivity on the loading amount of TiO_2 on Bi_2WO_6 [27]. Significantly, the CH_4 selectivity represents a volcano-like profile with the increase of TiO_2 content. Very recently, Yan et al. pointed that the intensity of interfacial interactions affects the CO selectivity of CO_2 photoreduction over $\text{Cs}_3\text{Bi}_2\text{Br}_9/\text{hierarchically porous BiVO}_4$ (CBB/HP-BVO) heterojunctions [28]. Despite frequent observations on the fluctuation of product selectivity with components' ratio in the previous reports [26–30], the underlying mechanism, however, has been ignored and unclear to date.

In this study, a $\text{Co}_3\text{O}_4/\text{ZnIn}_2\text{S}_4$ hollow hetero-nanocube (HHNC) structure comprised of Co_3O_4 hollow nanocubes (HNCs) and ZnIn_2S_4 nanoparticles (NPs) has been precisely constructed as a model system for visible-light-driven CO_2 photoreduction. The $\text{Co}_3\text{O}_4/\text{ZnIn}_2\text{S}_4$ HHNCs keep the internal surfaces of Co_3O_4 HNCs exposed to some extent with the increase of ZnIn_2S_4 loading amount, which provides good platform for studying the component ratio-dependent product selectivity evolution. It was found that both photocatalytic activity and product selectivity vary with the components' ratio. The photocatalytic activity takes a volcano-like evolution profile, while the CH_4 selectivity monotonously declines with the increase of ZnIn_2S_4 content. A combined analysis of in-situ spectroscopies and theoretical calculations reveals the origins of photocatalytic activity and product selectivity evolution, which is closely associated with the IEIs between Co_3O_4 HNCs and ZnIn_2S_4 NPs. In particular, the IEIs were also found to play a crucial role in the selectivity modulation. Furthermore, the IEIs-mediated selectivity evolution was verified by another similar model system of $\text{Co}_3\text{O}_4/\text{CeO}_2$ HHNCs constructed by the same strategy to $\text{Co}_3\text{O}_4/\text{ZnIn}_2\text{S}_4$ HHNCs, indicating a certain universality of the IEI effect. Taken together, this work unveils the effects of IEIs on photocatalysis from both catalytic activity and production selectivity for the first time. In particular, the IEI-mediated selectivity evolution provides new insights into the component ratio-dependent selectivity for heterogeneous photocatalysis.

2. Experimental

2.1. Materials

Cobaltous nitrate hexahydrate ($\text{Co}(\text{NO}_3)_2 \cdot 6 \text{H}_2\text{O}$, $\geq 99\%$), zinc nitrate hexahydrate ($\text{Zn}(\text{NO}_3)_2 \cdot 6 \text{H}_2\text{O}$, AR), indium nitrate hydrate ($\text{In}(\text{NO}_3)_3 \cdot x\text{H}_2\text{O}$, $\geq 99.9\%$), sodium sulfate (Na_2SO_4 , $\geq 98\%$), $\text{K}_3[\text{Fe}(\text{CN})_6]$

(AR), KCl (AR), thioacetamide (TAA, AR), hexadecyl trimethyl ammonium bromide (CTAB, AR), 2-methylimidazole (2-MI, $\geq 98\%$), absolute ethanol (AR), ethylene glycol (EG, AR), and Nafion solution (5.0 wt%, in lower aliphatic alcohols and water). All the chemicals were purchased from Sinopharm Chemical Reagent Co., Ltd. (China) and directly used without further purification. Deionized water was used throughout the work.

2.2. Synthesis of ZIF-67

Typically, 0.292 g of $\text{Co}(\text{NO}_3)_2 \cdot 6\text{H}_2\text{O}$ was dissolved in 10 mL distilled water containing 5 mg of CTAB to obtain solution A; solution B was obtained by dissolving 4.54 g of 2-MI in 70 mL of distilled water. The suspension A was quickly poured into solution B, the resultant mixture was stirred for 20 min and centrifuged. The precipitate was washed four times with ethanol and dried at 60°C in air for 12 h.

2.3. Synthesis of Co_3O_4 HNCs

Co_3O_4 HNCs were obtained by annealing ZIF-67 in air at 350°C for 2 h with a ramp rate of 1°C min^{-1} .

2.4. Synthesis of $\text{Co}_3\text{O}_4/\text{ZnIn}_2\text{S}_4$ HHNCs

15 mg of Co_3O_4 HNCs were dispersed in 30 mL EG with ultrasonication for 30 min. Then, 0.6 mmol $\text{Zn}(\text{NO}_3)_2 \cdot 6\text{H}_2\text{O}$, 1.2 mmol $\text{In}(\text{NO}_3)_3 \cdot x\text{H}_2\text{O}$, and 2.4 mmol TAA were dispersed into the above suspension under stirring. The resultant mixture was transferred into a 50 mL of Teflon-lined stainless-steel autoclave and kept at 160°C for 12 h. After cooling to ambient temperature, the precipitate was collected by centrifugation, washed with absolute ethanol for three times, and dried at 60°C for 12 h. The obtained sample was denoted as $\text{Co}_3\text{O}_4/\text{ZnIn}_2\text{S}_4$ -6. To adjust the loading amount of ZnIn_2S_4 , the dosage of $\text{Zn}(\text{NO}_3)_2 \cdot 6\text{H}_2\text{O}$, $\text{In}(\text{NO}_3)_3 \cdot x\text{H}_2\text{O}$, and TAA with a fixed molar ratio of 1:2:4 was set as one-third, two-third, and four-third times that of $\text{Co}_3\text{O}_4/\text{ZnIn}_2\text{S}_4$ -6 to obtain different $\text{Co}_3\text{O}_4/\text{ZnIn}_2\text{S}_4$ -y samples, where $y = 2, 4$, and 8, respectively.

2.5. Synthesis of ZnIn_2S_4 NPs

0.6 mmol $\text{Zn}(\text{NO}_3)_2 \cdot 6\text{H}_2\text{O}$, 1.2 mmol $\text{In}(\text{NO}_3)_3 \cdot x\text{H}_2\text{O}$, and 2.4 mmol TAA were dissolved into 30 mL of EG under stirring. The solution was transferred into a 50 mL of Teflon-lined stainless-steel autoclave and kept at 120°C for 6 h. After cooling to ambient temperature, the product was collected by centrifugation, washed with ethanol, and dried at 60°C for 12 h.

Other experimental details including material characterizations, photophysical and (photo)electrochemical measurements, photocatalytic CO_2 reduction experiments, and theoretical calculations, can be found in the Appendix A. [Supplementary data](#).

3. Results and discussion

3.1. Composition and Microstructure of $\text{Co}_3\text{O}_4/\text{ZnIn}_2\text{S}_4$ HHNCs

$\text{Co}_3\text{O}_4/\text{ZnIn}_2\text{S}_4$ HHNCs were prepared via a two-step method (Fig. 1a). First, bare cobalt-organic framework (ZIF-67) was synthesized as a cubic-structure precursor, which was calcined in air at 350°C for 2 h to obtain Co_3O_4 HNCs. Then, $\text{Co}_3\text{O}_4/\text{ZnIn}_2\text{S}_4$ HHNCs were prepared via a solvothermal reaction of EG solution containing $\text{Zn}(\text{NO}_3)_2$, $\text{In}(\text{NO}_3)_3$, TAA, and the as-synthesized Co_3O_4 HNCs. As shown in Fig. S1a, the as-synthesized ZIF-67 appears a typical cubic structure with a grain size of about 500 nm. The single-phase constitution of the as-synthesized ZIF-67 is validated by its X-ray diffraction (XRD) pattern (Fig. S1b). The Field-emission scanning electron microscopy (FESEM) images of Co_3O_4 HNCs, ZnIn_2S_4 NPs, and $\text{Co}_3\text{O}_4/\text{ZnIn}_2\text{S}_4$ HHNCs are shown in Fig. S2. Co_3O_4 HNCs keep the cubic structure of ZIF-67 but become rough

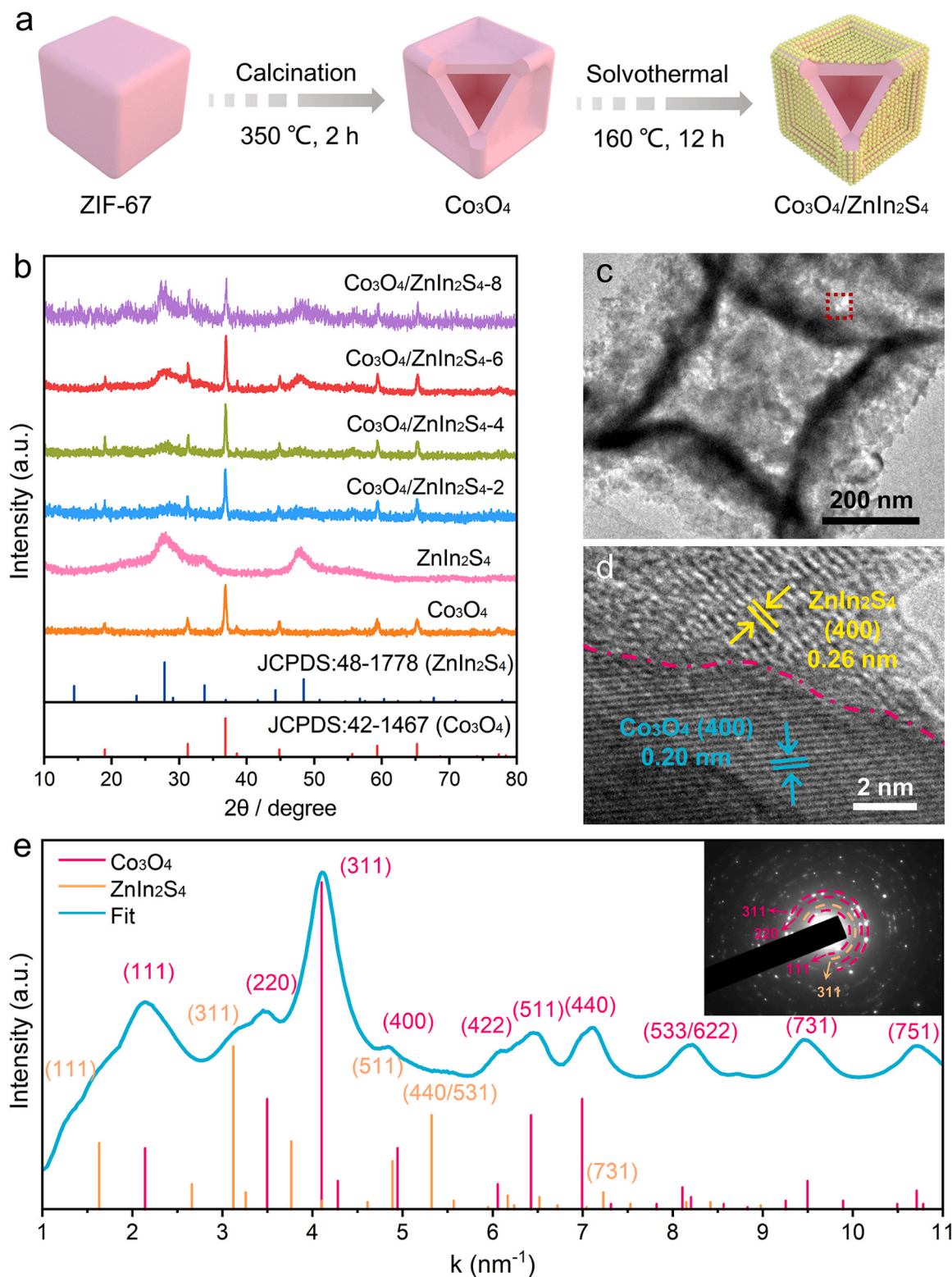


Fig. 1. (a) Schematic illustration of the synthetic process of the $\text{Co}_3\text{O}_4/\text{ZnIn}_2\text{S}_4$ HHNCs. (b) XRD patterns of the as-prepared Co_3O_4 HNCs, ZnIn_2S_4 NPs, and $\text{Co}_3\text{O}_4/\text{ZnIn}_2\text{S}_4$ - y ($y = 2, 4, 6$, and 8) HHNCs, (c) TEM and (d) HRTEM images of the $\text{Co}_3\text{O}_4/\text{ZnIn}_2\text{S}_4$ -6 HHNCs. (e) Averaged position and intensity of diffraction rings in the SAED pattern (inset) of the $\text{Co}_3\text{O}_4/\text{ZnIn}_2\text{S}_4$ -6 HHNCs.

surface made of small NPs derived from the Co-oxo clusters in ZIF-67 in the annealing process (Fig. S2a). Additionally, all the $\text{Co}_3\text{O}_4/\text{ZnIn}_2\text{S}_4$ - y HHNCs also maintain cubic morphology but appear covered by some NPs, and these NPs gradually increase with the y value (Fig. S2b-e), implying successful loading of ZnIn_2S_4 NPs on Co_3O_4 HNCs. Without

Co_3O_4 HNCs as supports, the as-prepared ZnIn_2S_4 sample exhibits a typical morphology of disordered NP structure (Fig. S2f). The XRD analyses verify the desirable phase constitution of Co_3O_4 HNCs, ZnIn_2S_4 NPs, and $\text{Co}_3\text{O}_4/\text{ZnIn}_2\text{S}_4$ HHNCs (Fig. 1b), where Co_3O_4 and ZnIn_2S_4 correspond to a cubic structure (space group: $Fd\bar{3}m$, JCPDS:42-1467 and

space group: $Fd\bar{3}m$, JCPDS: 48–1778, respectively). Moreover, the weak noisy peak at $2\theta = 22.5^\circ$ can be indexed to face-centered cubic ZnS. The appearance of a trace of ZnS is ascribed to the most addition of $\text{Zn}(\text{NO}_3)_2 \cdot 6\text{H}_2\text{O}$, $\text{In}(\text{NO}_3)_3 \cdot x\text{H}_2\text{O}$, and TAA for preparing $\text{Co}_3\text{O}_4/\text{ZnIn}_2\text{S}_4$ -8 HHNCs with the highest loading amount of ZnIn_2S_4 , which results in local reaction heterogeneity and thus formation of a trace of ZnS. Note that the impurity ZnS cannot be detected in the $\text{Co}_3\text{O}_4/\text{ZnIn}_2\text{S}_4$ - y ($y = 2, 4$, and 6) HHNCs, indicating that the impurity phase has little influence on photocatalytic performance and photocatalytic process. Besides, the appearance of the noisy peak in XRD patterns might be ascribed to the remained organics derived from ZIF-67. Note that Raman is more sensitive towards short-range ordering than XRD [31,32], the phase purity of Co_3O_4 HNCs and $\text{Co}_3\text{O}_4/\text{ZnIn}_2\text{S}_4$ HHNCs is also supported by their Raman spectra, as shown in Fig. S3. All the Raman bands can be well indexed to spinel structure Co_3O_4 in Co_3O_4 HNCs and $\text{Co}_3\text{O}_4/\text{ZnIn}_2\text{S}_4$ HHNCs without impurity signals [13]. The absence of Raman signals from ZnIn_2S_4 NPs is due to strong photoluminescence (PL) emission, which is discussed later.

The hollow structure, phase constitution, and elemental distribution of $\text{Co}_3\text{O}_4/\text{ZnIn}_2\text{S}_4$ HHNCs were further investigated by transmission electron microscopy (TEM) technique. The TEM image reveals a body cavity in a $\text{Co}_3\text{O}_4/\text{ZnIn}_2\text{S}_4$ HHNC (Fig. 1c), while the shells of Co_3O_4 HNCs appear distorted, likely due to shrink of six faces towards interior during calcination process. Moreover, a cover of the surface of Co_3O_4 HNCs by a coating verify successful loading of ZnIn_2S_4 NPs. The high-resolution TEM (HRTEM) image exhibits a clear interface separating two sets of lattice fringes (Fig. 1d), one of which was well indexed to the (400) planes of spinel-structure Co_3O_4 , the other one corresponds to the (400) planes of cubic ZnIn_2S_4 . The selected-area electron diffraction (SAED) image shows a set of irregular diffraction rings corresponding to polycrystalline aggregates (inset of Fig. 1e), where each ring exhibits an uneven brightness and diameter, indicating preferential orientation and nonuniform grain size in Co_3O_4 HNCs [33,34]. According to the previous report [35], the reciprocal spacings of the SAED pattern and their relative intensity along with an integrated intensity-spacing profile were obtained, as shown in Fig. 1e. A set of composite diffraction pattern containing cubic Co_3O_4 and ZnIn_2S_4 can be observed, in which main diffraction peaks were well assigned to Co_3O_4 , while the signal fluctuation of Co_3O_4 and some weak peaks are closely associated with the diffraction from ZnIn_2S_4 phase, with no impurity signal detected. Like Raman, SAED is also more sensitive to short-range ordering than XRD [31,36], thereby the phase constitution of $\text{Co}_3\text{O}_4/\text{ZnIn}_2\text{S}_4$ HHNCs is well verified. In addition, the scanning TEM-energy dispersive X-ray spectroscopy (STEM-EDS) images illustrate uniform distribution of Co, O, Zn, In, and S elements throughout the adjacent HHNCs (Fig. S4). To disclose the porous characteristics, N_2 adsorption-desorption curves were recorded, as shown in Fig. S5. All the samples present a type-IV isotherm with similar hysteresis loops, and the specific surface area was determined as $90 \text{ m}^2 \text{ g}^{-1}$ for ZnIn_2S_4 NPs, about four times higher as that of Co_3O_4 HNCs ($22 \text{ m}^2 \text{ g}^{-1}$) (Fig. S5a and b). As expected, the specific surface area of $\text{Co}_3\text{O}_4/\text{ZnIn}_2\text{S}_4$ HHNCs present a compromise result, gradual increasing from 55 to $86 \text{ m}^2 \text{ g}^{-1}$ with the loading amount of ZnIn_2S_4 (Fig. S5c–f). The significant difference of specific surface area between ZnIn_2S_4 NPs and Co_3O_4 HNCs is related to their grain size. According to the main diffraction peak of ZnIn_2S_4 and Co_3O_4 in Fig. 1b, the average grain size is calculated using Scherrer formula to be 275 nm for Co_3O_4 HNCs and 82 nm for ZnIn_2S_4 NPs. The smaller grain size endows ZnIn_2S_4 NPs with higher specific surface area. Moreover, the pore diameter distribution diagram shows the presence of predominant mesopore structure in all the samples while a gradual decreased average pore size with the increase of ZnIn_2S_4 content.

The surface composition and chemical states of elements in bare Co_3O_4 HNCs, ZnIn_2S_4 NPs, and $\text{Co}_3\text{O}_4/\text{ZnIn}_2\text{S}_4$ HHNCs were revealed by X-ray photoelectron spectroscopy (XPS). The survey XPS clearly shows, apart from signals of adventitious carbon, Co and O elements in bare Co_3O_4 HNCs, Zn, In, and S elements in ZnIn_2S_4 NPs, and all the identified

elements in $\text{Co}_3\text{O}_4/\text{ZnIn}_2\text{S}_4$ HHNCs (Fig. S6a), and no impurity elements were detected. The atomic percentage of these elements was listed in Table S1. The atomic ratios of Zn, In, and S are close to the theoretical value of ZnIn_2S_4 , while the atomic ratios of Co and O are higher than the theoretical value (0.75), implying more Co sites exposed on Co_3O_4 surface [37]. However, for $\text{Co}_3\text{O}_4/\text{ZnIn}_2\text{S}_4$ HHNCs, the exorbitant content of ZnIn_2S_4 indicates ZnIn_2S_4 NPs mostly distributed on the surface of Co_3O_4 HNCs. For bare ZnIn_2S_4 NPs, the Zn 2p high-resolution spectrum is shown in Fig. S6b, which depicts a doublet at 1022.2 and 1045.3 eV with a splitting energy of 23.1 eV, corresponding to divalent Zn species [38,39]. Similarly, the In 3d spectrum displays two symmetry peaks at 445.1 and 452.6 eV, being consistent with trivalent In (Fig. S6c) [39,40]. The S 2p spectrum was deconvoluted into two peaks at 161.7 and 162.9 eV, corresponding to S $2p_{3/2}$ and S $2p_{1/2}$ of S^{2-} , respectively (Fig. S6d) [41]. For bare Co_3O_4 HNCs, the deconvolution analysis on Co 2p spectrum reveals the presence of Co^{2+} with a doublet at 781.5 and 797.1 eV and Co^{3+} with a doublet at 779.4 and 794.9 eV (Fig. S6e) [42]. The O 1s spectrum indicates the lattice oxygen at 530.0 eV as predominate oxygen species as well as the presence of adsorbed hydroxyls (OH_{ads}) at 531.9 eV and bridged oxygen (O_{b}) at 531.1 eV (Fig. S6f) [43]. The reduction in signal of lattice oxygens in HNCs can be ascribed to the cover of ZnIn_2S_4 NPs on Co_3O_4 HNCs, which shields the XPS signals from Co_3O_4 to some extent under condition that the detectable depth of XPS is no more than 10 nm. Note that the IELs between Co_3O_4 and ZnIn_2S_4 are not reflected by the XPS data, since the E_{F} difference between Co_3O_4 HNCs and ZnIn_2S_4 NPs is not such large (0.04 eV, determined by the ultraviolet photoemission spectroscopy (UPS) analysis later) that the transferred electrons across the interfaces are limited. Besides, XPS is a typical analysis technique for surface element constitution and their chemical states. The IELs mainly affect the binding energies of atoms at the interfaces below the ZnIn_2S_4 phase, the distance between interface and surface weakens the XPS signals from the interfacial atoms to some extent. Therefore, the apparent XPS binding energy mostly reflects the signals of surface atoms, and is close to that of pure phases under the limited IELs.

The IELs within $\text{Co}_3\text{O}_4/\text{ZnIn}_2\text{S}_4$ HHNCs were studied by DFT, the structure models of bare Co_3O_4 , ZnIn_2S_4 , and $\text{Co}_3\text{O}_4/\text{ZnIn}_2\text{S}_4$ heterojunctions are shown in Fig. S7 and Fig. 2a. The model of $\text{Co}_3\text{O}_4/\text{ZnIn}_2\text{S}_4$ heterojunctions is constructed based on the HRTEM observation, where the interface is mostly formed by the contact between $\text{Co}_3\text{O}_4(400)$ and $\text{ZnIn}_2\text{S}_4(400)$ facets. For cubic crystals, the family of {400} facets are equivalent to that of the {001} facets. Compared to bare Co_3O_4 , the work function of $\text{Co}_3\text{O}_4(001)$ face is significantly reduced for $\text{Co}_3\text{O}_4/\text{ZnIn}_2\text{S}_4$, which is conducive to electron transfer from Co_3O_4 surface to adsorbed substrate molecules and thus favors photoreduction half-reactions [44]. Moreover, $\text{Co}_3\text{O}_4/\text{ZnIn}_2\text{S}_4$ exhibits a large potential step between Co_3O_4 and ZnIn_2S_4 across the interface, which will induce IELs (Fig. 2b and c). The charge density difference of $\text{Co}_3\text{O}_4/\text{ZnIn}_2\text{S}_4$ heterojunctions shows a charge redistribution along the interface with electron depletion at the side of Co_3O_4 and electron accumulation on the ZnIn_2S_4 side, accompanied by the formation of interfacial electric field (IEF) pointing from Co_3O_4 to ZnIn_2S_4 (Fig. 2d). Fig. 2e and f show the electrostatic potential mapping of bare Co_3O_4 and $\text{Co}_3\text{O}_4/\text{ZnIn}_2\text{S}_4$. Clearly, the electrostatic potential difference within $\text{Co}_3\text{O}_4/\text{ZnIn}_2\text{S}_4$ is larger than that of bare Co_3O_4 . According to the previous study [45], the large electrostatic potential difference supports the formation of strong IELs and IEF, which helps to separate photogenerated carriers for photocatalysis. Additionally, the comparison of density of state between bare Co_3O_4 and $\text{Co}_3\text{O}_4/\text{ZnIn}_2\text{S}_4$ reveals that an interfacial defect state contributed by Co, O, Zn, and S 2p orbitals near the E_{F} is formed, which enhances the interfacial conductivity for photogenerated carrier transfer (Fig. S8).

3.2. Photocatalytic CO_2 reduction performance

CO_2 photoreduction experiments were carried out in a gas-solid system under visible-light irradiation ($\lambda > 420 \text{ nm}$) using Co_3O_4 HNCs,

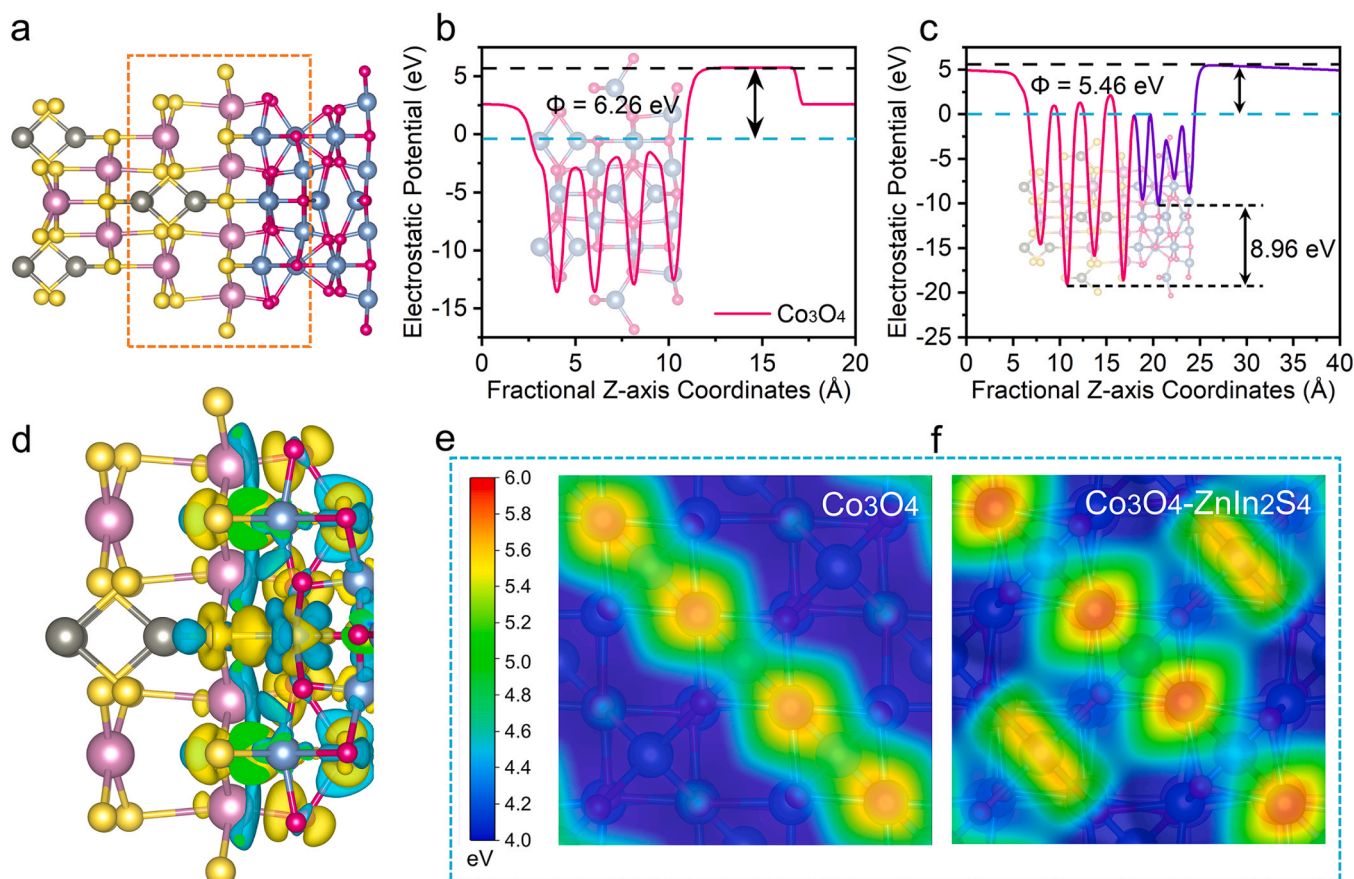


Fig. 2. (a) Structure Model of $\text{Co}_3\text{O}_4/\text{ZnIn}_2\text{S}_4$ heterojunctions. Electrostatic potentials of (b) bare Co_3O_4 and (c) $\text{Co}_3\text{O}_4/\text{ZnIn}_2\text{S}_4$ heterojunctions. (d) Calculated differential charge density at the $\text{Co}_3\text{O}_4/\text{ZnIn}_2\text{S}_4$ interface. The electron-density isosurface was plotted at $0.001 \text{ e}/\text{bohr}^3$. The yellow and blue regions represent electron accumulation and depletion, respectively. Calculated 2D electrostatic potential mapping of (e) $\text{Co}_3\text{O}_4(001)$ and (f) $\text{Co}_3\text{O}_4(001)/\text{ZnIn}_2\text{S}_4$ heterojunctions.

ZnIn_2S_4 NPs, and $\text{Co}_3\text{O}_4/\text{ZnIn}_2\text{S}_4$ HHNCs as catalysts. It was found that CO and CH_4 are main products, while no other gaseous or liquid products were detected, as confirmed by the ^1H nuclear magnetic resonance (^1H NMR) spectroscopy of liquid phases (Fig. S9a). As shown in Fig. 3a and b, Co_3O_4 HNCs enable both CO and CH_4 evolution but show the lowest CO_2 photoreduction activity in total. In contrast, ZnIn_2S_4 NPs display more active in CO evolution than that of CH_4 evolution. Compared to the two single-phase catalysts, $\text{Co}_3\text{O}_4/\text{ZnIn}_2\text{S}_4$ -6 HHNCs exhibit an outstanding photoactivity, especially for CH_4 evolution, delivering a single-carbon (C_1) compound production rate of $51.1 \mu\text{mol g}^{-1} \text{ h}^{-1}$ with a CH_4 product selectivity of 65.9% (Fig. 3c). The apparent quantum yield (AQY) of $\text{Co}_3\text{O}_4/\text{ZnIn}_2\text{S}_4$ -6 was determined under various monochromatic light, as shown in Fig. S10. The AQY gradually decreases with the increase of irradiation wavelength, which matches with the UV-vis diffuse reflectance spectrum (UV-vis DRS). The highest AQY is 0.83% at 400 nm. Interestingly, the C_1 compound production rate manifests a volcano-like profile with the increase of ZnIn_2S_4 content. Upon loading ZnIn_2S_4 , the CH_4 selectivity gradually decreases in terms of both product and electron selectivity (Fig. 3d). A series of control experiments show no C_1 compounds were detected under various conditions including in dark, using argon (Ar) gas to replace CO_2 , and without photocatalyst or H_2O (Fig. 3e), verifying real photocatalysis of CO_2 with H_2O on $\text{Co}_3\text{O}_4/\text{ZnIn}_2\text{S}_4$ HHNCs under irradiation and the protons in the detected CH_4 from H_2O molecules in the photocatalysis. No oxygen gas is detected in the photocatalysis process, due to the following two reasons. One is a great difference of detection line between O_2 and hydrocarbons (CO, CH_4 , and so on) on Shimadzu Gas Chromatograph GC-2014 by thermal conductivity detector (TCD) and flame ionization detector (FID), respectively. The former only detects O_2

with a concentration of $> 50 \text{ ppm}$, while the latter can detect hydrocarbons with a concentration of $> 1 \text{ ppm}$. According to the C_1 -compound production rate of $\text{Co}_3\text{O}_4/\text{ZnIn}_2\text{S}_4$ -6 HHNCs, the stoichiometric oxygen evolution ratio was calculated to be 28 ppm in 4 h, significantly lower than the detection line. In addition, the generated oxygen easily suffers from photoadsorption [46,47], resulting in further decrease in the concentration of oxygen in the gaseous products. As the cases in the most studies on CO_2 photoreduction [48–51], no specific oxygen yield is given when the theoretical yield is not high enough. Furthermore, the isotopic labeling experiment was also carried out under identical test conditions by replacing $^{12}\text{CO}_2$ with $^{13}\text{CO}_2$ as the substrate, the obtained mass spectra of $m/z = 17$ and 29 correspond to $^{13}\text{CH}_4$ and ^{13}CO , respectively, confirming the resource of detected C_1 compounds indeed from the used CO_2 gas (Fig. S9b).

The durability of $\text{Co}_3\text{O}_4/\text{ZnIn}_2\text{S}_4$ HHNC photocatalysts was assessed by a cyclic photocatalytic test with each run of 4 h under identical conditions, as shown in Fig. 3f. The CH_4 evolution rate remains roughly unchanged in a total of 16 h. Furthermore, the XRD, FESEM, and XPS analyses on the recycled $\text{Co}_3\text{O}_4/\text{ZnIn}_2\text{S}_4$ HHNCs show that the elemental composition and chemical state, phase constitution, and hollow cubic structure were kept during CO_2 reduction process (Fig. S11 and S12). In a word, $\text{Co}_3\text{O}_4/\text{ZnIn}_2\text{S}_4$ HHNCs exhibit good stability for CO_2 photoreduction to CH_4 .

3.3. Origins of photoactivity evolution

To unveil the enhanced photocatalytic activity, the effects of specific surface area on photoactivity were further examined. For this purpose, the surface-area-normalized photoactivity (moles of evolved CO and

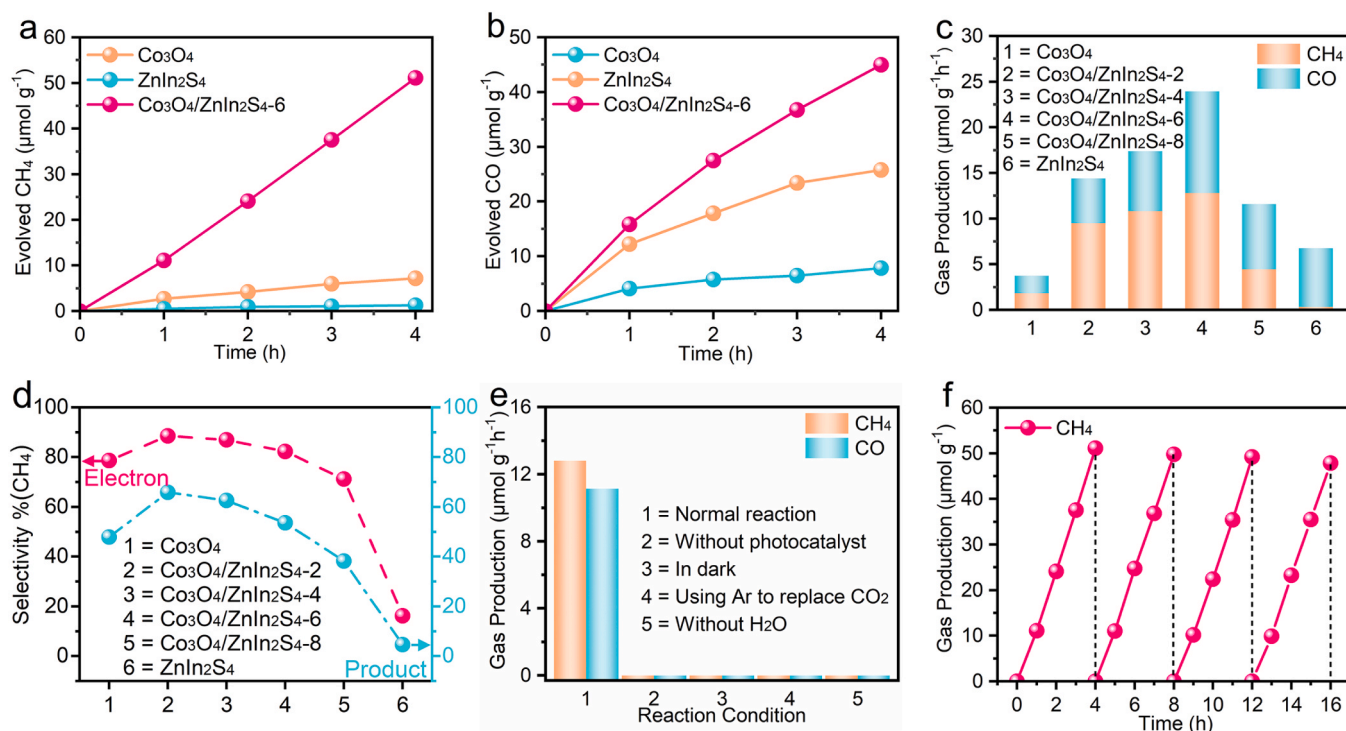


Fig. 3. Time courses of photocatalytic (a) CH₄ and (b) CO evolution on different catalysts under visible-light irradiation ($\lambda > 420$ nm), (c) CH₄ and CO evolution rates over different samples, (d) electron selectivity and product selectivity of CH₄ evolution over different samples, (e) CO₂ photoreduction activity under various reaction conditions, (f) cyclic tests of the Co₃O₄/ZnIn₂S₄-6 HHNCs for photocatalytic CH₄ evolution.

CH₄ per unit surface area of catalysts per unit time) were obtained by dividing the mass-normalized photoactivity (moles of evolved CO and CH₄ per unit mass of catalysts per unit time) by the specific surface area, as shown in Fig. S13a. As seen, the trend of surface-area-normalized photoactivity also manifests a volcano-like profile, being consistent with that of mass-normalized photoactivity. Given that both CO and CH₄ with different portion evolve on all the catalysts and the number of photoelectrons for CO and CH₄ evolution reactions is also different (2 versus 8), it is practically unreasonable to investigate the photoactivity evolution in terms of surface-area-normalized activity. To solve this issue, electron utilization rate as a proof of concept, defined as the electron number (moles) produced for CO₂ reduction per unit surface area of catalysts per unit time, is proposed as a new photoactivity parameter representing the intrinsic photocatalytic activity. The parameter is suitable for all photocatalysts in principle, especially for multiphase materials with variable product selectivity. As shown in Fig. S13b, Co₃O₄ HNCs manifest higher electron utilization rate in total as well as better CH₄ selectivity than ZnIn₂S₄ NPs, indicating that Co₃O₄ HNCs possess a high intrinsic photoactivity towards CO₂ reduction than ZnIn₂S₄ NPs. The intrinsic photoactivity and CH₄ selectivity are drastically promoted when ZnIn₂S₄ NPs are loaded on Co₃O₄ NCs, owing to the IEs evidenced by the DFT calculations. Moreover, Co₃O₄/ZnIn₂S₄-2, 4, and 6 HHNCs display a very close photoactivity in terms of their electron utilization rate, indicating that IEs is the key factor governing photoactivity for Co₃O₄/ZnIn₂S₄ HHNCs with moderate loading of ZnIn₂S₄. In this regard, the electron utilization rate is more brilliant in revealing the intrinsic photoactivity than previously used mass- and specific-surface-area normalized photoactivity. In contrast, an excess loading of ZnIn₂S₄ NPs is detrimental to the photoactivity of Co₃O₄/ZnIn₂S₄ HHNCs, possibly due to the severe cover of Co₃O₄ by ZnIn₂S₄ NPs, making the surface properties of Co₃O₄/ZnIn₂S₄-8 close to bare ZnIn₂S₄. Anyway, the greatly improved CH₄ selectivity cannot be rationalized by the effect of specific surface area. In addition, the effect of CO₂ adsorption capacity is examined by recording CO₂ adsorption curves, as shown in Fig. S14. Although Co₃O₄/ZnIn₂S₄-6 HHNCs present

the highest CO₂ uptake compared to Co₃O₄ HNCs and ZnIn₂S₄ NPs, while the increment does not match with those of their photoactivity, indicating the enhanced photoactivity is irrelevant to CO₂ adsorption capacity.

The influences of light absorption and carrier separation on photoactivity were assessed by UV-vis DRS and a series of photophysical and (photo)electrochemical measurements. As shown in Fig. S15a, Co₃O₄ HNCs show a full spectrum response in the wavelength range of 200–800 nm, while ZnIn₂S₄ NPs only absorbs the light with wavelength lower than ~500 nm, which is not in agreement with the higher C₁ production rate on ZnIn₂S₄ NPs relative to Co₃O₄ HNCs. The band gap was determined as 1.46 and 2.59 eV for bare Co₃O₄ HNCs and ZnIn₂S₄ NPs, according to their Tauc plots (Fig. S15b). Owing to the presence of Co₃O₄ component, all the Co₃O₄/ZnIn₂S₄ HHNCs show full spectrum response with slight difference in absorption intensity, which is also inconsistent with the trend of their photoactivity. These results allow us to correlate the enhanced photoactivity with the separation efficiency of photogenerated carriers. The photocurrent response of these samples is shown in Fig. S16a, upon irradiation, single-phase Co₃O₄ HNCs and ZnIn₂S₄ NPs show significantly lower photocurrent signals than all the Co₃O₄/ZnIn₂S₄ HHNCs. In particular, the Co₃O₄/ZnIn₂S₄-6 HHNCs display the highest photocurrent signal. Moreover, the PL and transient PL spectra (TRPL) spectra reveal that Co₃O₄/ZnIn₂S₄-6 HHNCs have the weakest PL emission and shorter average PL lifetime as compared to Co₃O₄ HNCs and ZnIn₂S₄ NPs as well as other Co₃O₄/ZnIn₂S₄ HHNCs (Fig. S16b and c). According to the previous literature [52], the shortening of the PL lifetimes is ascribed to the charge separation process through heterogenous interfaces. In addition, the electrochemical impedance spectroscopy (EIS) illustrates Co₃O₄/ZnIn₂S₄-6 HHNCs having the smallest Nernst semicircle among these catalysts (Fig. S16d). Taken together, the separation of photogenerated carriers and their transfer kinetics are greatly improved for Co₃O₄/ZnIn₂S₄ HHNCs in comparison with single-phase counterparts, due to the IEs, which accounts for the enhanced photoactivity of Co₃O₄/ZnIn₂S₄ HHNCs relative to bare Co₃O₄ HNCs and ZnIn₂S₄ NPs.

Based on the above results, a plausible mechanism behind the volcano-like evolution profile can be rationalized by combining with the previous studies on heterojunctions for photocatalysis [53–55]. Both bare Co_3O_4 HNCs and ZnIn_2S_4 NPs show low photocatalytic activity due to poor charge separation efficiency. When ZnIn_2S_4 NPs are loaded on Co_3O_4 HNCs, closely contacted interfaces are formed between Co_3O_4 and ZnIn_2S_4 , accompanied by the IELs and the formation of IEF. The interfaces act as channels to IEF-driven photogenerated carrier transfer. More loading amount of ZnIn_2S_4 , more intimate interfaces formed. When the number of interfaces reaches saturation, the specific surface area will be responsible for the photoactivity evolution of different $\text{Co}_3\text{O}_4/\text{ZnIn}_2\text{S}_4$ HHNCs. However, the excess loading of ZnIn_2S_4 severely covers Co_3O_4 HNCs, which not only shields the light absorption of Co_3O_4 HNCs, but also extend the distance of photogenerated carriers' diffusion to catalyst surface [53], leading to degenerate photoelectric efficiency and increased resistance for interface charge transfer. As a result, the photoactivity of $\text{Co}_3\text{O}_4/\text{ZnIn}_2\text{S}_4$ -8 HHNCs is slightly higher than that of ZnIn_2S_4 NPs.

3.4. Influence of IELs on charge transfer pathway under irradiation

To reveal the IEL-mediated charge transfer under irradiation, the band alignment of $\text{Co}_3\text{O}_4/\text{ZnIn}_2\text{S}_4$ -6 HHNCs was investigated by a combined analysis of Mott-Schottky plots and UPS. The Mott-Schottky measurements were made to assess the nature of semiconductors and the electrochemical potential (versus reversible hydrogen electrode, RHE) of conduction band minimum (CBM) of Co_3O_4 HNCs and ZnIn_2S_4 NPs, that is E_{CB} , as shown in Fig. S15c and d, respectively. The positive slopes indicate n-type nature of Co_3O_4 HNCs and ZnIn_2S_4 NPs. Although Co_3O_4 is frequently reported as p-type electrocatalysts, while the n-type nature of Co_3O_4 as photocatalysts have been recognized [56,57]. That is, the semiconducting type of Co_3O_4 is dependent on the specific preparation method. The E_{CB} was determined to be -0.65 and -0.47 eV for Co_3O_4 HNCs and ZnIn_2S_4 NPs, respectively, while the potential (E_{VB}) of valence band maximum (VBM) was calculated from $E_{\text{CB}} + E_g$ as 0.81 and 2.12 eV. Moreover, the positions of E_f were determined based on their work function (ϕ) measured by ultraviolet UPS, as illustrated in

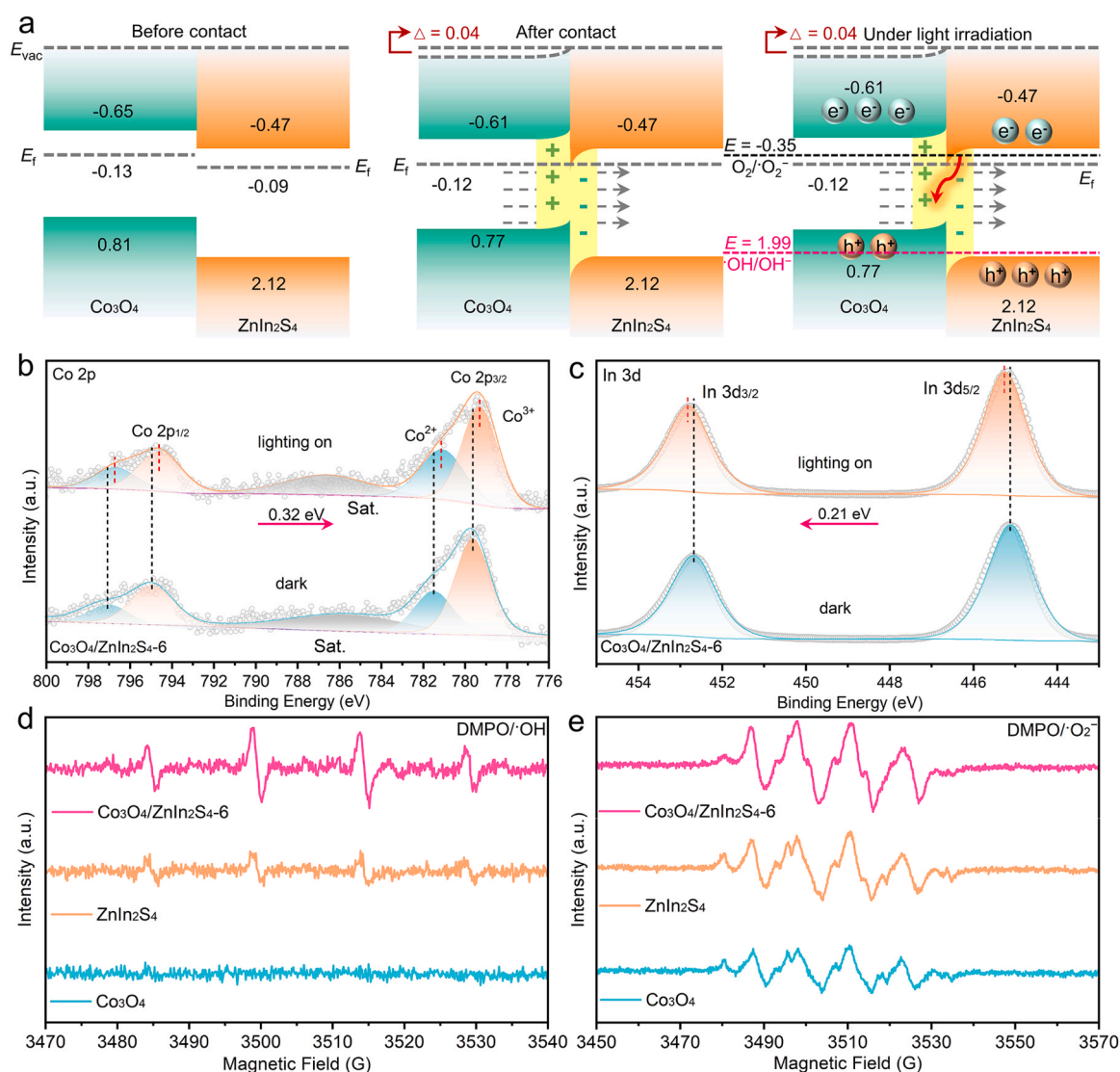


Fig. 4. (a) Schematic illustration of formation of the $\text{Co}_3\text{O}_4/\text{ZnIn}_2\text{S}_4$ heterojunction. E_{vac} , vacuum level. The plus and minus signs indicate the positively and negatively charged regions at the junction, respectively, whereas the grey dashed arrows indicate the direction of IEF. The red arrows show the photoinduced electron transfer direction. Δ refers to the E_f difference at the junction. The energy levels are in volt (versus RHE). (b) Co 2p and (f) In 3d high-resolution XPS spectra of $\text{Co}_3\text{O}_4/\text{ZnIn}_2\text{S}_4$ -6 HHNCs with and without irradiation. The values above the pink arrows indicate the shift magnitude of XPS peaks. EPR results of (d) $\bullet\text{OH}$ and (e) $\bullet\text{O}_2^{\bullet}$ free radicals trapped by DMPO in (d) aqueous and (e) methylbenzene suspension of $\text{Co}_3\text{O}_4/\text{ZnIn}_2\text{S}_4$ -6 HHNCs, Co_3O_4 HNCs, and ZnIn_2S_4 NPs after 15 min of visible light illumination.

Fig. S17a. The Φ was calculated by subtracting the secondary electron cutoff (E_{cutoff}) from the excitation energy (21.22 eV) to be 4.72 and 4.76 eV for Co_3O_4 HNCs and ZnIn_2S_4 NPs, respectively. The difference of Φ between Co_3O_4 and ZnIn_2S_4 is larger than the energy uncertainty of 0.02 eV for UPS, indicating that Co_3O_4 HNCs indeed have smaller Φ than ZnIn_2S_4 NPs. Given the free electron level set to be 0.00 eV as the vacuum level, the corresponding E_f was determined to be -4.72 and -4.76 eV, respectively. Finally, the E_f values were converted to electrochemical potentials in volts (V versus RHE) according to the following equation [58],

$$E(\text{vs RHE}) = -4.44 - E(\text{vs vacuum}) - 0.059\text{pH} \quad (1)$$

The band alignment of Co_3O_4 HNCs and ZnIn_2S_4 NPs is illustrated in **Fig. 4a**. Upon contact in dark, the E_f difference drives electron transfer from Co_3O_4 to ZnIn_2S_4 for Fermi equilibrium and thus induces an IEF pointing from Co_3O_4 to ZnIn_2S_4 , resulting in IEIs. The E_f of $\text{Co}_3\text{O}_4/\text{ZnIn}_2\text{S}_4$ HHNCs was determined by UPS analysis to lie between those of Co_3O_4 and ZnIn_2S_4 , as shown in **Fig. S17b**. This result is consistent with the Φ reduction of Co_3O_4 within heterojunction compared to bare Co_3O_4 , demonstrated by the DFT calculations. Upon irradiation, both of two components are excited, constrained by the IEF, photoelectrons transfer from ZnIn_2S_4 to Co_3O_4 , obeying a S-scheme pathway. Accordingly, CO_2 conversion mainly occur on Co_3O_4 component, while the

photooxidation half-reaction mostly proceeds over ZnIn_2S_4 . In-situ irradiated XPS was employed to examine the actual electron transfer pathway. Compared to that in dark, the Co 2p spectrum of $\text{Co}_3\text{O}_4/\text{ZnIn}_2\text{S}_4$ HHNCs exhibits an evident shift towards lower binding energy by -0.32 eV under irradiation (**Fig. 4b**), which is contrary to the cases of In 3d and Zn 2p spectra ($+0.21$ and $+0.16$ eV, respectively) (**Fig. 4c and S18**). Note that all the shift magnitudes are significantly higher than the energy uncertainty of 0.05 eV for XPS. Collectively, these results confirm electron transfer from ZnIn_2S_4 to Co_3O_4 within $\text{Co}_3\text{O}_4/\text{ZnIn}_2\text{S}_4$ HHNCs under irradiation.

To further confirm the presence of IEIs within $\text{Co}_3\text{O}_4/\text{ZnIn}_2\text{S}_4$ HHNCs and the electron transfer pathway under irradiation, free radical trapping experiments were conducted, as shown in **Fig. 4d and e**. As the CBM potentials of both Co_3O_4 HNCs and ZnIn_2S_4 NPs are enough negative for oxygen reduction ($\text{O}_2/\cdot\text{O}_2^-$), while $\cdot\text{OH}$ free radicals can be only generated on the surface of ZnIn_2S_4 NPs [59]. As expected, the EPR spectrum of Co_3O_4 HNCs is silent, while ZnIn_2S_4 NPs display a weak EPR signal corresponding to the adduct of DMPO/ $\cdot\text{OH}$. Significantly, $\text{Co}_3\text{O}_4/\text{ZnIn}_2\text{S}_4$ -6 HHNCs exhibit enhanced EPR signal in comparison with ZnIn_2S_4 NPs, indicating photogenerated holes accumulating on the surface of ZnIn_2S_4 for $\text{Co}_3\text{O}_4/\text{ZnIn}_2\text{S}_4$. On the other hand, Co_3O_4 HNCs and ZnIn_2S_4 NPs present nearly equivalent EPR signal corresponding to $\cdot\text{O}_2^-$ free radicals, while the EPR signal is enhanced for $\text{Co}_3\text{O}_4/\text{ZnIn}_2\text{S}_4$ -6

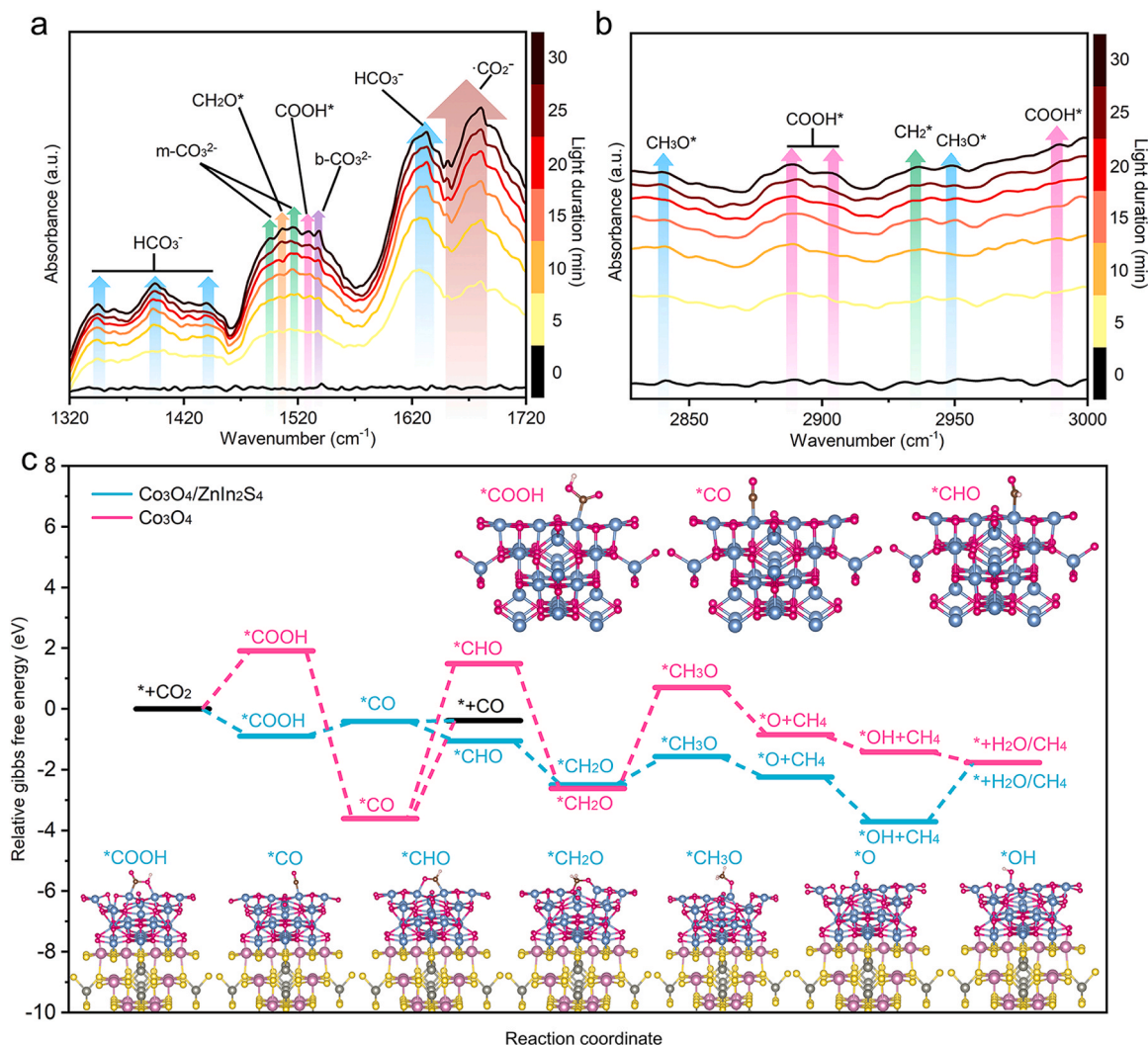


Fig. 5. (a and b) In-situ DRIFTS of the $\text{Co}_3\text{O}_4/\text{ZnIn}_2\text{S}_4$ -6 HHNCs exposed to a mixture gas of He, CO_2 , and H_2O with and without irradiation. (c) Reaction pathways for CO_2 photocatalysis on bare Co_3O_4 and $\text{Co}_3\text{O}_4/\text{ZnIn}_2\text{S}_4$ heterojunctions and calculated Gibbs free energies of reaction intermediates. The Co, O, In, Zn, S, C, and H atoms are represented by blue, pink, lilac, gray, yellow, brown, and white balls, respectively.

HHNCs, indicating IEI-induced electron accumulation within the heterojunctions under irradiation. Taken together, the IEIs between within $\text{Co}_3\text{O}_4/\text{ZnIn}_2\text{S}_4$ HHNCs and the proposed charge transfer pathway are well confirmed. Moreover, the active sites for CO_2 photoreduction are deservedly located at the surface of Co_3O_4 within the heterojunctions.

3.5. IEIs-mediated selectivity

To unravel the IEIs-mediated selectivity, the main reaction intermediates in CO_2 photoreduction over $\text{Co}_3\text{O}_4/\text{ZnIn}_2\text{S}_4$ HHNCs were monitored by in-situ diffuse reflectance infrared Fourier transform spectra (in-situ DRIFTS), (Fig. 5a and b). Prior to irradiation, $\text{Co}_3\text{O}_4/\text{ZnIn}_2\text{S}_4$ -6 HHNCs were exposed to a mixture gas of He, CO_2 , and a trace of water vapor in dark for reaching adsorption equilibrium, the obtained Fourier transform infrared spectroscopy (FTIR) signals were taken as background and deducted as baseline. Upon irradiation, multiple reaction intermediates were observed. The adsorption bands at 1632 and 1341–1440, 1494 and 1517, and 1539 cm^{-1} correspond to HCO_3^- , monodentate carbonate (m-CO_3^{2-}), bicarbonate (b-CO_3^{2-}) species, respectively [60,61], indicating the co-adsorption and reactions of CO_2 and H_2O molecules on catalyst surface. Moreover, the emergence of CO_2 species at 1642–1680 cm^{-1} and its increasing signal with irradiation time demonstrate easy single-electron reduction of the adsorbed CO_2 by photoelectrons [60]. Furthermore, the conversion of the adsorbed CO_2 is confirmed by the appearance of key intermediate $^*\text{COOH}$ at 1529, 2889, 2905 and 2989 cm^{-1} [26,61–63]. A series of hydrocarbon intermediates including $^*\text{CH}_2\text{O}$ at 1506 cm^{-1} , $^*\text{CH}_3\text{O}$ at 2840 and 2949 cm^{-1} , and $^*\text{CH}_2$ at 2938 cm^{-1} verify the relatively favorable hydrogenation process of $^*\text{CO}$ to CH_4 . As comparisons, the in-situ DRIFTS of both Co_3O_4 HNCs and ZnIn_2S_4 NPs are recorded under the same condition to that of $\text{Co}_3\text{O}_4/\text{ZnIn}_2\text{S}_4$ HHNCs. As shown in Fig. S19a and b, as the case of $\text{Co}_3\text{O}_4/\text{ZnIn}_2\text{S}_4$ -6 HHNCs, $^*\text{COOH}$ and hydrocarbon intermediates could be observed for Co_3O_4 HNCs, indicating that both CO and CH_4 can be steadily evolved on the surface of Co_3O_4 HNCs. In contrast, there is hardly signals from hydrocarbon intermediates seen on the surface of ZnIn_2S_4 NPs (Fig. S19c and d), indicating ZnIn_2S_4 NPs are active in evolving CO rather than CH_4 . These results are consistent with the experimental results.

Based on the in-situ DRIFTS results, a plausible reaction pathway was determined for the CO_2 conversion, as shown in Fig. 5c. For both bare Co_3O_4 and $\text{Co}_3\text{O}_4/\text{ZnIn}_2\text{S}_4$ heterojunctions, the active sites for CO_2 conversion are located on Co atoms at the surface of Co_3O_4 . The corresponding Gibbs free energies (ΔG) of and reaction intermediates on the Co_3O_4 and $\text{Co}_3\text{O}_4/\text{ZnIn}_2\text{S}_4$ models described above were respectively calculated by DFT. With bare Co_3O_4 as the catalyst, the generation of intermediate $^*\text{COOH}$ is thermodynamically unfavored. Moreover, both desorption and hydrogenation of $^*\text{CO}$ are significantly uphill reactions, though, the formation of $^*\text{CO}$ is an obvious exothermic process. These results account for low catalytic activity and poor selectivity of bare Co_3O_4 HNCs for CO_2 reduction. By comparison, with $\text{Co}_3\text{O}_4/\text{ZnIn}_2\text{S}_4$ heterojunctions as the photocatalyst, the electron-enriched Co_3O_4 component favors the generation of $^*\text{COOH}$ with a negative ΔG . In particular, the hydrogenation of $^*\text{CO}$ to $^*\text{CHO}$ becomes significantly favorable in contrast to its desorption to gaseous CO , though the formation of $^*\text{CO}$ is a slightly uphill reaction. Furthermore, the continuous hydrogenation processes of $^*\text{CHO}$ to $^*\text{OH}+\text{CH}_4$ correspond to a series of exothermic reactions, resulting in preferential CH_4 evolution on $\text{Co}_3\text{O}_4/\text{ZnIn}_2\text{S}_4$. Taken together, it is concluded that the IEIs tune the electronic structure of Co_3O_4 within $\text{Co}_3\text{O}_4/\text{ZnIn}_2\text{S}_4$, making it more suitable for CH_4 evolution.

Given that two and eight electrons required for the conversions of CO_2 to CO and CH_4 , respectively, the possibility of multielectron-induced methanation may also be practicable. The photocurrent spectra reveal that $\text{Co}_3\text{O}_4/\text{ZnIn}_2\text{S}_4$ -6 has the strongest electron accumulation on Co_3O_4 but shows the second worst CH_4 selectivity. Moreover, all the proposed elementary reactions for CO_2 to CH_4 only require

one electron, which is not dependent on the electron accumulation. Collectively, the possibility of multielectron-induced methanation can be ruled out.

In-situ near atmospheric pressure XPS (NAP-XPS) spectra of the C 1s and O 1s regions were recorded to verify the photocatalysis process of CO_2 with H_2O over $\text{Co}_3\text{O}_4/\text{ZnIn}_2\text{S}_4$ HHNCs under different conditions. Fig. 6a presents the in-situ changes in C 1s core level spectra. In ultra-high vacuum (UHV), only three kinds of carbon species are identified on catalyst surface: C-C, C-O, and C=O at binding energy of 285.3, 286.9, and 288.1 eV, respectively. After high-purity CO_2 gas was pumped into the system, reaching a pressure of 0.5 mbar in dark and adsorption equilibrium. Multiple new components were observed, including gas-phase CO_2 at 293.3 eV, $\text{CO}_2^{\cdot-}$ and HCO_3^- species at 291.7 and 290.8 eV, respectively. Interestingly, an obvious peak at 283.7 eV, which was well assigned to carbon-metal (C-M) bonds according to the previous reports [43,64–67], indicating effective adsorption and activation of CO_2 molecules on the metal sites of catalysts. Upon irradiation, apart from species observed in the dark, an obvious reduction in intensity occurs for the C-M and C=O species, implying their chemical conversion (Table S2). In particular, the appearance of C-H bonds at 283.0 eV indicates favorable hydrogenation reactions and CO_2 -to- CH_4 conversion [64,68]. On the other hand, the O 1s core level spectrum in UHV condition was fitted using four components: adsorbed water ($\text{H}_2\text{O}_{\text{ads}}$), adsorbed hydroxyls (OH_{ads}), surface bridging O (O_{b}), and Co-O species (Fig. 6b and Table S3), in agreement with the XPS results of O 1s spectra in Fig. S6f and S12f. The introduction of CO_2 gases into the system significantly reduces the content of $\text{H}_2\text{O}_{\text{ads}}$ by the reactions of H_2O and CO_2 molecules, leading to the emergence of carbonates at 532.4 eV as well as more exposure of surface Co-O species acting as active centers, in addition to the component of CO_2 gas [67]. Moreover, a trace number of C-O species at 534.5 eV suggests slight dissociation of the adsorbed CO_2 molecules [64]. Under irradiation, the C-O species significantly increase, indicating visible-driven CO_2 activation and conversion, agreeing with the results of the C 1s spectra analysis.

To examine the validity of IEIs-mediated activity and selectivity, we further use CeO_2 to replace the ZnIn_2S_4 component, constructing $\text{Co}_3\text{O}_4/\text{CeO}_2$ HHNCs. The selection of CeO_2 is due to its high CO selectivity towards CO_2 photoreduction according to the previous reports [69–71]. The FESEM and XRD analyses reveal the successful preparation of $\text{Co}_3\text{O}_4/\text{CeO}_2$ HHNCs with different components' ratio (Figs. S21 and S22). As expected, bare CeO_2 shows low CO_2 -to- CO rate but high CO selectivity (Fig. S23a and b), while $\text{Co}_3\text{O}_4/\text{CeO}_2$ HHNCs deliver a significantly increased C_1 -compound production rate due to IEIs, which presents a volcano-like profile with the increase of CeO_2 loading amount (Fig. S23c). Moreover, the CH_4 selectivity synchronously declines (Fig. S23d), resembling the case of $\text{Co}_3\text{O}_4/\text{ZnIn}_2\text{S}_4$ HHNCs. Taken together, the IEIs-mediated activity and selectivity are verified undoubtedly, which exhibits a certain universality.

3.6. Photocatalytic mechanism

Base on the above analyses, a plausible mechanism for CO_2 photoreduction on $\text{Co}_3\text{O}_4/\text{ZnIn}_2\text{S}_4$ HHNCs was summarized in Scheme 1, the intimate contact of Co_3O_4 HNCs and ZnIn_2S_4 NPs results in strong IEIs and thus the formation of IEF, which tunes the electronic structure of Co_3O_4 , making it favorable for continuous hydrogenation process of CO_2 and thus promoting CH_4 selectivity as compared to bare Co_3O_4 and ZnIn_2S_4 . Under visible-light irradiation, both Co_3O_4 and ZnIn_2S_4 are excited, with the assistance of IEF, photoelectrons transfer from ZnIn_2S_4 to Co_3O_4 for CO_2 reduction in terms of S-scheme pathway. CO_2 molecules are preferentially adsorbed on the Co sites by forming C-Co bonds, accompanied by a bending of the adsorbed CO_2 (Step 1). The bent CO_2 is converted into the $^*\text{COOH}$ intermediate by receiving one proton and one photoelectron (Step 2). The $^*\text{COOH}$ dehydrates (Step 3) and transforms into $^*\text{CHO}$ (Step 4) with continuous aid of proton-electron pairs. The subsequent multistep hydrogenation processes lead to the formation

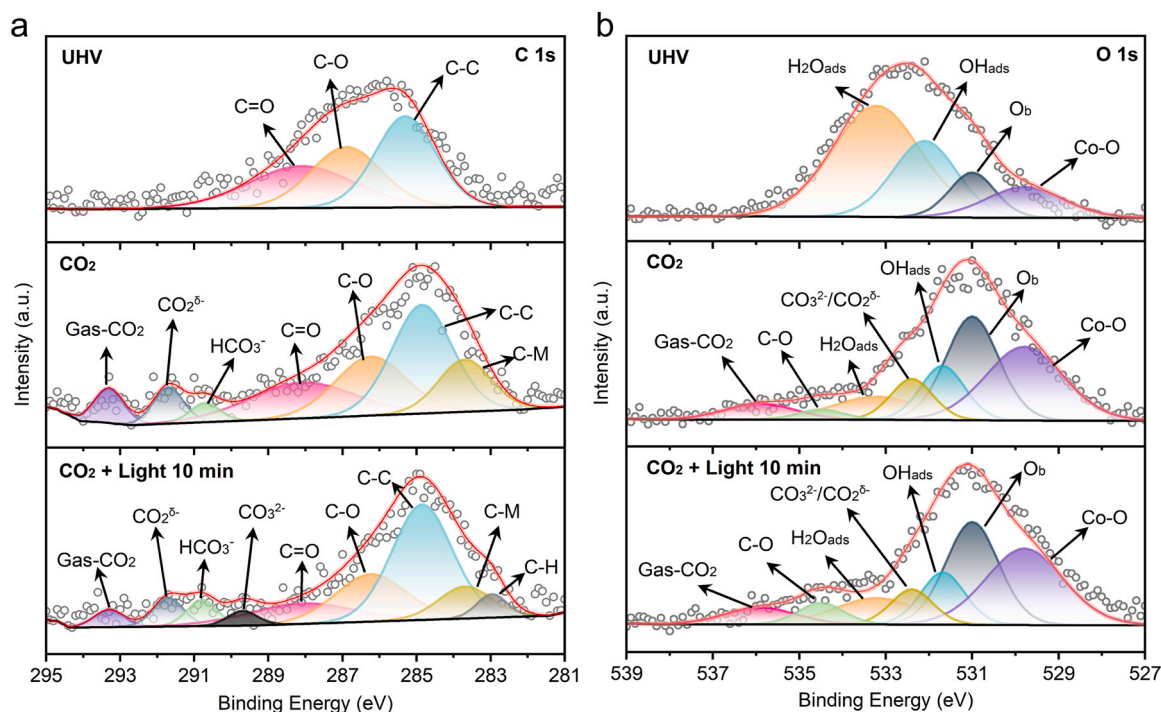
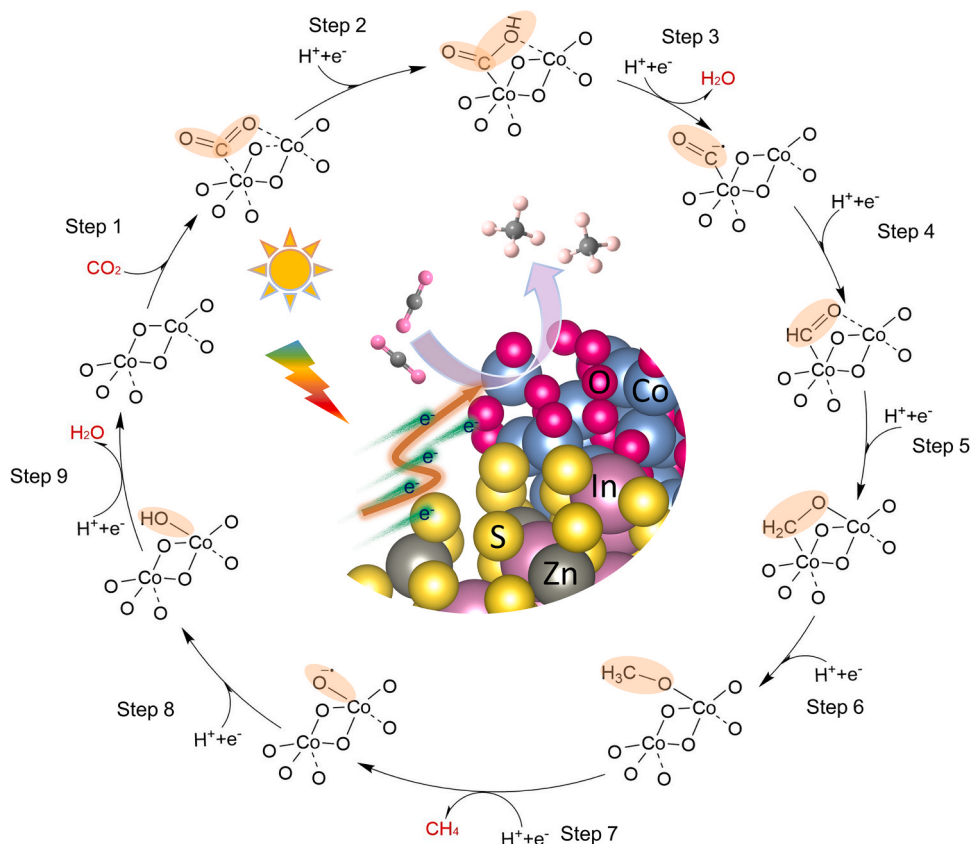


Fig. 6. In-situ NAP-XPS spectra of (a) C 1s and (b) O 1s regions recorded for the $\text{Co}_3\text{O}_4/\text{ZnIn}_2\text{S}_4$ HHNCs under the following conditions (from top to bottom): UHV; 0.5 mbar CO₂ atmosphere; 0.5 mbar CO₂ atmosphere and light illumination.



Scheme 1. Proposed reaction pathway for photocatalytic reduction of CO₂ to CH₄ using $\text{Co}_3\text{O}_4/\text{ZnIn}_2\text{S}_4$ HHNCs with IELs. For the ball-and-stick models, the gray, pink, and white balls represent C, O, and H atoms, respectively.

of *CH_2O and *CH_3O intermediates (Step 5 and 6), until one methane molecule is formed and released, leaving a O-bonded Co site (Step 7). The negatively charged center recovers by two hydrogenation processes under irradiation (Step 8 and 9) for next photocatalytic circle.

4. Conclusion

In summary, $Co_3O_4/ZnIn_2S_4$ HHNCs have been well constructed via a two-step method of ZIF-67 transformation followed by a solvothermal reaction and proposed for efficient visible-light-driven CO_2 photoreduction. Bare Co_3O_4 HNCs enable both CO and CH_4 evolution, while $ZnIn_2S_4$ NPs favor CO generation. As the loading amount of $ZnIn_2S_4$ increases, the C_1 -compound generation rate of $Co_3O_4/ZnIn_2S_4$ HHNCs manifests a volcano-like profile. In particular, the CH_4 selectivity monotonously reduces. The photoactivity evolution is governed by IEIs-promoted carrier separation and the effects of specific surface area under moderate loading of $ZnIn_2S_4$, while the CH_4 selectivity is closely associated with the IEIs between Co_3O_4 and $ZnIn_2S_4$, which tunes the electronic structure of Co_3O_4 and lowers the energy barrier of key intermediate *CHO , making consequent hydrogenation processes easier. The IEIs-mediated activity and selectivity are validated by a similar model catalyst Co_3O_4/CeO_2 HHNCs, which further exhibit a certain universality of the IEI effect. This work has unveiled the interacting mechanism underlying the product selectivity evolution and shed new light on the manipulation of multiple-phase photocatalytic products.

CRedit authorship contribution statement

Hu Yong: Conceptualization, Funding acquisition, Supervision, Writing – review & editing. **Zhao Yuanyuan:** Formal analysis. **Ni Maomao:** Investigation, Methodology. **Xu Hengyue:** Software, Validation. **Guo Changfa:** Funding acquisition, Writing – review & editing. **Cheng Chao:** Data curation, Investigation, Visualization, Writing – original draft.

Declaration of Competing Interest

The authors declared that there is no conflict of interest.

Data Availability

The authors do not have permission to share data.

Acknowledgments

This work is financially supported by the National Natural Science Foundation of China (22272150, 22102145), the Major Program of Zhejiang Provincial Natural Science Foundation of China (LD22B030002), Zhejiang Provincial Ten Thousand Talent Program (2021R51009), and the Zhejiang Provincial Natural Science Foundation of China (LY22B030012). The calculations were carried out on high performance supercomputer of Zhejiang Normal University.

Appendix A. Supporting information

Supplementary data associated with this article can be found in the online version at [doi:10.1016/j.apcatb.2024.123705](https://doi.org/10.1016/j.apcatb.2024.123705).

References

- [1] T. Inoue, A. Fujishima, S. Konishi, K. Honda, Photoelectrocatalytic reduction of carbon dioxide in aqueous suspensions of semiconductor powders, *Nature* 277 (1979) 637–638, <https://doi.org/10.1038/277637a0>.
- [2] S. Wang, X. Han, Y. Zhang, N. Tian, T. Ma, H. Huang, Inside-and-out semiconductor engineering for CO_2 photoreduction: from recent advances to new trends, *Small Struct.* 2 (2021) 2000061, <https://doi.org/10.1002/sstr.202000061>.
- [3] X. Shi, Y. Huang, Y. Bo, D. Duan, Z. Wang, J. Cao, G. Zhu, W. Ho, L. Wang, T. Huang, Y. Xiong, Highly selective photocatalytic CO_2 methanation with water vapor on single-atom platinum-decorated defective carbon nitride, *Angew. Chem. Int. Ed.* 61 (2022) e202203063, <https://doi.org/10.1002/ange.202203063>.
- [4] S.N. Habisreutinger, L. Schmidt-Mende, J.K. Stolarczyk, Photocatalytic reduction of CO_2 on TiO_2 and other semiconductors, *Angew. Chem. Int. Ed.* 52 (2013) 7372–7408, <https://doi.org/10.1002/anie.201207199>.
- [5] Z. Guo, G. Chen, C. Cometto, B. Ma, H. Zhao, T. Groizard, L. Chen, H. Fan, W. Man, S. Yiu, K. Lau, T. Lau, M. Robert, Selectivity control of CO versus $HCOO^-$ production in the visible-light-driven catalytic reduction of CO_2 with two cooperative metal sites, *Nat. Catal.* 2 (2019) 801–808, <https://doi.org/10.1038/s41929-019-0331-6>.
- [6] X. Chang, T. Wang, J. Gong, CO_2 photo-reduction: insights into CO_2 activation and reaction on surfaces of photocatalysts, *Energy Environ. Sci.* 9 (2016) 2177–2196, <https://doi.org/10.1039/C6EE00383D>.
- [7] W. Tu, Y. Zhou, Z. Zou, Photocatalytic conversion of CO_2 into renewable hydrocarbon fuels: state-of-the-art accomplishment, challenges, and prospects, *Adv. Mater.* 26 (2014) 4607–4626, <https://doi.org/10.1002/adma.201400087>.
- [8] W. Gao, S. Li, H. He, X. Li, Z. Cheng, Y. Yang, J. Wang, Q. Shen, X. Wang, Y. Xiong, Y. Zhou, Z. Zou, Vacancy-defect modulated pathway of photoreduction of CO_2 on single atomically thin $AgInP_2S_6$ sheets into olefin gas, *Nat. Commun.* 12 (2021) 4747, <https://doi.org/10.1038/s41467-021-25068-7>.
- [9] L. Liu, Z. Wang, J. Zhang, O. Ruzimuradov, K. Dai, J. Low, Tunable interfacial charge transfer in a 2D–2D composite for efficient visible-light-driven CO_2 conversion, *Adv. Mater.* 35 (2023) 2300643, <https://doi.org/10.1002/adma.202300643>.
- [10] S. Karmakar, S. Barman, F.A. Rahimi, D. Rambabu, S. Nath, T.K. Maji, Confining charge-transfer complex in a metal-organic framework for photocatalytic CO_2 reduction in water, *Nat. Commun.* 14 (2023) 4508, <https://doi.org/10.1038/s41467-023-40117-z>.
- [11] R. Marschall, Semiconductor composites: strategies for enhancing charge carrier separation to improve photocatalytic activity, *Adv. Funct. Mater.* 24 (2014) 2421–2440, <https://doi.org/10.1002/adfm.201303214>.
- [12] W. Zhang, A.R. Mohamed, W.J. Ong, Z-scheme photocatalytic systems for carbon dioxide reduction: Where are we now? *Angew. Chem. Int. Ed.* 59 (2020) 22894–22915, <https://doi.org/10.1002/anie.201914925>.
- [13] M.E. Malefane, U. Feleni, P.J. Mafa, A.T. Kuvarega, Fabrication of direct Z-scheme $Co_3O_4/BiOI$ for ibuprofen and trimethoprim degradation under visible light irradiation, *Appl. Surf. Sci.* 514 (2020) 145940, <https://doi.org/10.1016/j.apsusc.2020.145940>.
- [14] Y. Bai, M. Li, X. Liu, J. Han, X. Zhu, Q. Ge, H. Wang, Ti^{3+} defective TiO_2/CdS Z-scheme photocatalyst for enhancing photocatalytic CO_2 reduction to C_1 – C_3 products, *Ind. Eng. Chem. Res.* 61 (2022) 8724–8737, <https://doi.org/10.1021/acs.iecr.2c01113>.
- [15] M. Hao, D. Wei, Z. Li, Rational design of an efficient S-scheme heterojunction of CdS/Bi_2WO_6 -S nanocomposites for photocatalytic CO_2 reduction, *Energy Fuels* 36 (2022) 11524–11531, <https://doi.org/10.1021/acs.energyfuels.2c01076>.
- [16] F. Li, X. Yue, Y. Liao, L. Qiao, K. Lv, Q. Xiang, Understanding the unique S-scheme charge migration in triazine/heptazine crystalline carbon nitride homojunction, *Nat. Commun.* 14 (2023) 3901, <https://doi.org/10.1038/s41467-023-39578-z>.
- [17] M. Ni, Y. Zhu, C. Guo, D.-L. Chen, J. Ning, Y. Zhong, Y. Hu, Efficient visible-light-driven CO_2 methanation with self-regenerated oxygen vacancies in $Co_3O_4/NiCo_2O_4$ hetero-nanocages: vacancy-mediated selective photocatalysis, *ACS Catal.* 13 (2023) 2502–2512, <https://doi.org/10.1021/acscatal.2c05577>.
- [18] M. Anagnostopoulou, A. Zindrou, T. Cottineau, A. Kafizas, C. Marchal, Y. Deligiannakis, V. Keller, K.C. Christoforidis, MOF-derived defective Co_3O_4 nanosheets in carbon nitride nanocomposites for CO_2 photoreduction and H_2 production, *ACS Appl. Mater. Interfaces* 15 (2023) 6817–6830, <https://doi.org/10.1021/acsami.2c19683>.
- [19] Y. Zhang, J. Li, W. Zhou, X. Liu, X. Song, S. Chen, H. Wang, P. Huo, Rational design of $Ag/CuO@ZnIn_2S_4$ S-scheme plasmonic photocatalyst for highly selective CO_2 conversion, *Appl. Catal. B-Environ.* 342 (2024) 123449, <https://doi.org/10.1016/j.apcatb.2023.123449>.
- [20] Y. Zhang, Y. Wu, L. Wan, H. Ding, H. Li, X. Wang, W. Zhang, Hollow core-shell $Co_9S_8@ZnIn_2S_4/CdS$ nanoreactor for efficient photothermal effect and CO_2 photoreduction, *Appl. Catal. B-Environ.* 311 (2022) 121255, <https://doi.org/10.1016/j.apcatb.2022.121255>.
- [21] L. Wang, D. Chen, S. Miao, F. Chen, C. Guo, P. Ye, J. Ning, Y. Zhong, Y. Hu, Nitric acid-assisted growth of $InVO_4$ nanobelts on protonated ultrathin C_3N_4 nanosheets as an S-scheme photocatalyst with tunable oxygen vacancies for boosting CO_2 conversion, *Chem. Eng. J.* 434 (2022) 133867, <https://doi.org/10.1016/j.cej.2021.133867>.
- [22] V. Giulimondi, S. Mitchell, J. Pérez-Ramírez, Challenges and opportunities in engineering the electronic structure of single-atom catalysts, *ACS Catal.* 13 (2023) 2981–2997, <https://doi.org/10.1021/acscatal.2c05992>.
- [23] X. Su, T. Xu, R. Ye, C. Guo, S.M. Wabaidur, D.L. Chen, S. Aftab, Y. Zhong, Y. Hu, One-pot solvothermal synthesis of In-doped amino-functionalized $UiO-66$ Zr-MOFs with enhanced ligand-to-metal charge transfer for efficient visible-light-driven CO_2 reduction, *J. Colloid Interf. Sci.* 646 (2023) 129–140, <https://doi.org/10.1016/j.jcis.2023.05.041>.
- [24] Z. Bi, R. Guo, X. Hu, J. Wang, X. Chen, W. Pan, Fabrication of a concave cubic Z-scheme $ZnIn_2S_4/Cu_2O$ heterojunction with superior light-driven CO_2 reduction performance, *Energy Fuels* 37 (2023) 6036–6048, <https://doi.org/10.1021/acs.energyfuels.3c00672>.
- [25] P. Su, X. Zhang, X. Hao, H. Liu, Z. Jin, Co_3O_4 modified $Mn_{0.2}Cd_{0.8}S$ with different shells forms p-n heterojunction to optimize energy/mass transfer for efficient

- photocatalytic hydrogen evolution, *Sep. Purif. Technol.* 285 (2022) 120318, <https://doi.org/10.1016/j.seppur.2021.120318>.
- [26] S. Liu, L. Chen, T. Liu, S. Cai, X. Zou, J. Jiang, Z. Mei, Z. Gao, H. Guo, Rich S vacant g-C₃N₄@CuInS₄ hollow heterojunction for highly efficient selective photocatalytic CO₂ reduction, *Chem. Eng. J.* 424 (2021) 130325, <https://doi.org/10.1016/j.cej.2021.130325>.
- [27] L. Collado, M. Gomez-Mendoza, M. García-Tecedor, F.E. Oropeza, A. Reynal, J. R. Durrant, D.P. Serrano, V.A. de la Peña O'Shea, Towards the improvement of methane production in CO₂ photoreduction using Bi₂WO₆/TiO₂ heterostructures, *Appl. Catal. B-Environ.* 324 (2023) 122206, <https://doi.org/10.1016/j.apcatb.2022.122206>.
- [28] B. Zhou, S. Xu, L. Wu, M. Li, Y. Chong, Y. Qiu, G. Chen, Y. Zhao, C. Feng, D. Ye, K. Yan, Strain-engineering of mesoporous Cs₃Bi₂Br₉/BiVO₄ S-scheme heterojunction for efficient CO₂ photoreduction, *Small* 19 (2023) 2302058, <https://doi.org/10.1002/smll.202302058>.
- [29] C. Guo, D. Chen, Y. Hu, Perspective on defective semiconductor heterojunctions for CO₂ photoreduction, *Langmuir* 38 (2022) 6491–6498, <https://doi.org/10.1021/acs.langmuir.2c00820>.
- [30] L. Li, X. Dai, D. Chen, Y. Zeng, Y. Hu, X.W.D. Lou, Steering catalytic activity and selectivity of CO₂ photoreduction to syngas with hydroxy-rich Cu₂S@R₀H-NiCo₂O₃ double-shelled nanoboxes, *Angew. Chem. Int. Ed.* 61 (2022) e202205839, <https://doi.org/10.1002/anie.202205839>.
- [31] S. Naghdi, A. Cherevan, A. Giesriegel, R. Guillet-Nicolas, S. Biswas, T. Gupta, J. Wang, T. Haunold, B.C. Bayer, G. Rupprechter, M.C. Toroker, F. Kleitz, D. Eder, Selective ligand removal to improve accessibility of active sites in hierarchical MOFs for heterogeneous photocatalysis, *Nat. Commun.* 13 (2022) 282, <https://doi.org/10.1038/s41467-021-27775-7>.
- [32] C. Adelhelm, M. Balden, M. Rinke, M. Stueber, Influence of doping (Ti, V, Zr, W) and annealing on the sp² carbon structure of amorphous carbon films, *J. Appl. Phys.* 105 (2009) 033522, <https://doi.org/10.1063/1.3075843>.
- [33] Z.R. Tian, J.A. Voigt, J. Liu, B. McKenzie, M.J. McDermott, M.A. Rodriguez, H. Konishi, H. Xu, Complex and oriented ZnO nanostructures, *Nat. Mater.* 2 (2003) 821–826, <https://doi.org/10.1038/nmat1014>.
- [34] S. Zhou, C. Zhang, J. Liu, Y. Liao, Y. Kong, Y. Xu, G. Chen, Formation of an oriented Bi₂WO₆ photocatalyst induced by in situ Bi reduction and its use for efficient nitrogen fixation, *Catal. Sci. Technol.* 9 (2019) 5562–5566, <https://doi.org/10.1039/C9CY00972H>.
- [35] C. Gammer, C. Mangler, C. Rentenberger, H.P. Karnthaler, Quantitative local profile analysis of nanomaterials by electron diffraction, *Scr. Mater.* 63 (2010) 312–315, <https://doi.org/10.1016/j.scriptamat.2010.04.019>.
- [36] B.C. Bayer, D.A. Bosworth, F.B. Michaeils, R. Blume, G. Habler, R. Abart, R. S. Weatherup, P.R. Kidambi, J.J. Baumberg, A. Knop-Gericke, R. Schloegl, C. Beatch, Z.H. Barber, J.C. Meyer, S. Hofmann, In situ observations of phase transitions in metastable nickel (carbide)/carbon nanocomposites, *J. Phys. Chem.* 120 (2016) 22571–22584, <https://doi.org/10.1021/acs.jpcc.6b01555>.
- [37] T. Ling, D. Yan, Y. Jiao, H. Wang, Y. Zheng, X. Zheng, J. Mao, X. Du, Z. Hu, M. Jaroniec, S. Qiao, Engineering surface atomic structure of single-crystal cobalt (II) oxide nanorods for superior electrocatalysis, *Nat. Commun.* 7 (2016) 12876, <https://doi.org/10.1038/ncomms12876>.
- [38] L. Wang, B. Cheng, L. Zhang, J. Yu, In situ irradiated XPS investigation on S-scheme TiO₂@ZnIn₂S₄ photocatalyst for efficient photocatalytic CO₂ reduction, *Small* 17 (2021) 2103447, <https://doi.org/10.1002/smll.202103447>.
- [39] H.T. Fan, Z. Wu, K.C. Liu, W.S. Liu, Fabrication of 3D CuS@ZnIn₂S₄ hierarchical nanocages with 2D/2D nanosheet subunits p-n heterojunctions for improved photocatalytic hydrogen evolution, *Chem. Eng. J.* 433 (2022) 134474, <https://doi.org/10.1016/j.cej.2021.134474>.
- [40] S. Wang, B.Y. Guan, X.W.D. Lou, Construction of ZnIn₂S₄-In₂O₃ hierarchical tubular heterostructures for efficient CO₂ photoreduction, *J. Am. Chem. Soc.* 140 (2018) 5037–5040, <https://doi.org/10.1021/jacs.8b02200>.
- [41] L. Huang, B. Li, B. Su, Z. Xiong, C. Zhang, Y. Hou, Z. Ding, S. Wang, Fabrication of hierarchical Co₃O₄@CdIn₂S₄ p-n heterojunction photocatalysts for improved CO₂ reduction with visible light, *J. Mater. Chem. A* 8 (2020) 7177–7183, <https://doi.org/10.1039/D0TA01817A>.
- [42] H. Ouyang, K. Song, J. Du, Z. Zhan, B. Tan, Creating chemisorption sites for enhanced CO₂ chemical conversion activity through amine modification of metalloporphyrin-based hypercrosslinked polymers, *Chem. Eng. J.* 431 (2022) 134326, <https://doi.org/10.1016/j.cej.2021.134326>.
- [43] L. Collado, P. Reñones, J. Feroso, F. Fresno, L. Garrido, V. Pérez-Dieste, C. Escudero, M.D. Hernández-Alonso, J.M. Coronado, D.P. Serrano, V.A. de la Peña O'Shea, The role of the surface acidic/basic centers and redox sites on TiO₂ in the photocatalytic CO₂ reduction, *Appl. Catal. B-Environ.* 303 (2022) 120931, <https://doi.org/10.1016/j.apcatb.2021.120931>.
- [44] A. Biswas, S. Nandi, N. Kamboj, J. Pan, A. Bhowmik, R.S. Dey, Alteration of electronic band structure via a metal-semiconductor interfacial effect enables high faradaic efficiency for electrochemical nitrogen fixation, *ACS Nano* 15 (2021) 20364–20376, <https://doi.org/10.1021/acsnano.1c08652>.
- [45] Y. Zhang, Y. Li, X. Xin, Y. Wang, P. Guo, R. Wang, B. Wang, W. Huang, A. J. Sobrido, X. Li, Internal quantum efficiency higher than 100% achieved by combining doping and quantum effects for photocatalytic overall water splitting, *Nat. Energy* 8 (2023) 504–514, <https://doi.org/10.1038/s41560-023-01242-7>.
- [46] S. Gong, G. Zhu, R. Wang, F. Rao, X. Shi, J. Gao, Y. Huang, C. He, M. Hojamberdiev, Synergistically boosting highly selective CO₂-to-CO photoreduction over BiOCl nanosheets via in-situ formation of surface defects and non-precious metal nanoparticles, *Appl. Catal. B-Environ.* 297 (2021) 120413, <https://doi.org/10.1016/j.apcatb.2021.120413>.
- [47] S.S. Tan, L. Zou, E. Hu, Photocatalytic reduction of carbon dioxide into gaseous hydrocarbon using TiO₂ pellets, *Catal. Today* 115 (2006) 269–273, <https://doi.org/10.1016/j.cattod.2006.02.057>.
- [48] T. Yan, N. Li, L. Wang, W. Ran, P.N. Duchesne, L. Wan, N.T. Nguyen, L. Wang, M. Xia, G.A. Ozin, Bismuth atom tailoring of indium oxide surface frustrated Lewis pairs boosts heterogeneous CO₂ photocatalytic hydrogenation, *Nat. Commun.* 11 (2020) 6095, <https://doi.org/10.1038/s41467-020-19997-y>.
- [49] J. Yu, J. Low, W. Xiao, P. Zhou, M. Jaroniec, Enhanced photocatalytic CO₂-reduction activity of anatase TiO₂ by coexposed {001} and {101} facets, *J. Am. Chem. Soc.* 136 (2014) 8839–8842, <https://doi.org/10.1021/ja5044787>.
- [50] L.L. Tan, W.J. Ong, S.P. Chai, A.R. Mohamed, Band gap engineered, oxygen-rich TiO₂ for visible light induced photocatalytic reduction of CO₂, *Chem. Commun.* 50 (2014) 6923–6926, <https://doi.org/10.1039/C4CC01304B>.
- [51] Y. Xiao, J. Liu, J. Leng, Z. Yin, Y. Yin, F. Zhang, C. Sun, S. Jin, Long-lived internal charge-separated state in two-dimensional metal-organic frameworks improving photocatalytic performance, *ACS Energy Lett.* 7 (2022) 2323–2330, <https://doi.org/10.1021/acseenergylett.2c00970>.
- [52] J. Yang, J. Jing, Y. Zhu, A full-spectrum porphyrin-fullerene D-A supramolecular photocatalyst with giant built-in electric field for efficient hydrogen production, *Adv. Mater.* 33 (2021) 2101026, <https://doi.org/10.1002/adma.202101026>.
- [53] J. Kosco, M. Bidwell, H. Cha, T. Martin, C.T. Howells, M. Sachs, D.H. Anjum, S. Gonzalez Lopez, L. Zou, A. Wadsworth, W. Zhang, L. Zhang, J. Tellam, R. Sougrat, F. Laquai, D.M. DeLongchamp, J.R. Durrant, I. McCulloch, Enhanced photocatalytic hydrogen evolution from organic semiconductor heterojunction nanoparticles, *Nat. Mater.* 19 (2020) 559–565, <https://doi.org/10.1038/s41563-019-0591-1>.
- [54] K.C. Kwon, S. Choi, K. Hong, D.M. Andoshe, J.M. Suh, C. Kim, K.S. Choi, J.H. Oh, S. Y. Kim, H.W. Jung, Tungsten disulfide thin film/p-type Si heterojunction photocathode for efficient photochemical hydrogen production, *MRS Commun.* 7 (2017) 272–279, <https://doi.org/10.1557/mrc.2017.37>.
- [55] L. Kong, Z. Jiang, H.H. Lai, R.J. Nicholls, T. Xiao, M.O. Jones, P.P. Edwards, Unusual reactivity of visible-light-responsive AgBr–BiOBr heterojunction photocatalysts, *J. Catal.* 293 (2012) 116–125, <https://doi.org/10.1016/j.jcat.2012.06.011>.
- [56] G. Qian, W. Lyu, X. Zhao, J. Zhou, R. Fang, F. Wang, Y. Li, Efficient photoreduction of diluted CO₂ to tunable syngas by Ni–Co dual sites through d-band center manipulation, *Angew. Chem. Int. Ed.* 61 (2022) e202210576, <https://doi.org/10.1002/anie.202210576>.
- [57] W. Lyu, Y. Liu, J. Zhou, D. Chen, X. Zhao, R. Fang, F. Wang, Y. Li, Modulating the reaction configuration by breaking the structural symmetry of active sites for efficient photocatalytic reduction of low-concentration CO₂, *Angew. Chem. Int. Ed.* 62 (2023) e202310733, <https://doi.org/10.1002/anie.202310733>.
- [58] T. Xu, X. Su, Y. Zhu, S. Khan, D.L. Chen, C. Guo, J. Ning, Y. Zhong, Y. Hu, One-pot solvothermal synthesis of flower-like Fe-doped In₂S₃/Fe₃S₄ S-scheme heteromicrospheres with enhanced interfacial electric field and boosted visible-light-driven CO₂ reduction, *J. Colloid Interf. Sci.* 629 (2023) 1027–1038, <https://doi.org/10.1016/j.jcis.2022.09.132>.
- [59] H.S. Moon, K.C. Hsiao, M.C. Wu, Y. Yun, Y.J. Hsu, K. Yong, Spatial separation of cocatalysts on Z-scheme organic/inorganic heterostructure hollow spheres for enhanced photocatalytic H₂ evolution and in-depth analysis of the charge-transfer mechanism, *Adv. Mater.* 35 (2023) 2200172, <https://doi.org/10.1002/adma.202200172>.
- [60] J. Sheng, Y. He, M. Huang, C. Yuan, S. Wang, F. Dong, Frustrated Lewis pair sites boosting CO₂ photoreduction on Cs₂CuBr₄ perovskite quantum dots, *ACS Catal.* 12 (2022) 2915–2926, <https://doi.org/10.1021/acscatal.2c00037>.
- [61] J. Sheng, Y. He, J. Li, C. Yuan, H. Huang, S. Wang, Y. Sun, Z. Wang, F. Dong, Identification of halogen-associated active sites on bismuth-based perovskite quantum dots for efficient and selective CO₂-to-CO photoreduction, *ACS Nano* 14 (2020) 13103–13114, <https://doi.org/10.1021/acsnano.0c04659>.
- [62] J. Xu, Z. Ju, W. Zhang, Y. Pan, J. Zhu, J. Mao, X. Zheng, H. Fu, M. Yuan, H. Chen, R. Li, Efficient infrared-light-driven CO₂ reduction over ultrathin metallic Ni-doped CoS₂ nanosheets, *Angew. Chem. Int. Ed.* 60 (2021) 8705–8709, <https://doi.org/10.1002/ange.202017041>.
- [63] T.C. Schilke, A.E. Fisher, A.T. Bell, In situ infrared study of methanol synthesis from CO₂/H₂ on titania and zirconia promoted Cu/SiO₂, *J. Catal.* 184 (1999) 144–156, <https://doi.org/10.1006/jcat.1999.2434>.
- [64] L. Collado, A. Reynal, F. Fresno, M. Barawi, C. Escudero, V. Perez-Dieste, J. M. Coronado, D.P. Serrano, J.R. Durrant, V.A. de la Peña O'Shea, Unravelling the effect of charge dynamics at the plasmonic metal/semiconductor interface for CO₂ photoreduction, *Nat. Commun.* 9 (2018) 4986, <https://doi.org/10.1038/s41467-018-07397-2>.
- [65] H. Blumh, M. Hävecker, A. Knop-Gericke, E. Kleimenov, R. Schlögl, D. Teschner, V. I. Bukhtiyarov, D.F. Ogletree, M. Salmeron, Methanol oxidation on a copper catalyst investigated using in situ X-ray photoelectron spectroscopy, *J. Phys. Chem. B* 108 (2004) 14340–14347, <https://doi.org/10.1021/jp040080j>.
- [66] X. Deng, A. Verdaguer, T. Herranz, C. Weis, H. Blumh, M. Salmeron, Surface chemistry of Cu in the presence of CO₂ and H₂O, *Langmuir* 24 (2008) 9474–9478, <https://doi.org/10.1021/la8011052>.
- [67] D. Ferrah, A.R. Haines, R.P. Galhenage, J.P. Bruce, A.D. Babore, A. Hunt, I. Waluyo, J.C. Hemminger, Wet chemical growth and thermocatalytic activity of Cu-based nanoparticles supported on TiO₂ nanoparticles/HOPG: In situ ambient pressure XPS study of the CO₂ hydrogenation reaction, *ACS Catal.* 9 (2019) 6783–6802, <https://doi.org/10.1021/acscatal.9b01419>.
- [68] G.E. Muilenberg, Handbook of X-ray photoelectron spectroscopy, Perkin-Elmer Corporation, Phys. Electron. Div., Minn. (1979) 38–42, <https://doi.org/10.1002/sia.740030412>.

- [69] Z. Wang, J. Zhu, X. Zu, Y. Wu, S. Shang, P. Ling, P. Qiao, C. Liu, J. Hu, Y. Pan, J. Zhu, Y. Sun, Y. Xie, Selective CO₂ photoreduction to CH₄ via Pd^{δ+}-assisted hydrodeoxygenation over CeO₂ nanosheets, *Angew. Chem. Int. Ed.* 61 (2022) e202203249, <https://doi.org/10.1002/anie.202203249>.
- [70] Z. Guan, Y. Chen, Y. Ding, J. Lin, Y. Zhao, Y. Jiao, G. Tian, Efficient charge transfer and CO₂ photoreduction of hierarchical CeO₂@SnS₂ heterostructured hollow spheres with spatially separated active sites, *Appl. Surf. Sci.* 592 (2022) 153192, <https://doi.org/10.1016/j.apsusc.2022.153192>.
- [71] H. Dong, L. Zhang, L. Li, W. Deng, C. Hu, Z.J. Zhao, J. Gong, Abundant Ce³⁺ ions in Au-CeO_x nanosheets to enhance CO₂ electroreduction performance, *Small* 15 (2019) 1900289, <https://doi.org/10.1002/sml.201900289>.